

# MineAgent: Towards Remote-Sensing Mineral Exploration with Multimodal Large Language Models

Anonymous ACL submission

## Abstract

Remote-sensing mineral exploration is critical for identifying economically viable mineral deposits, yet it poses significant challenges for multimodal large language models (MLLMs). These include limitations in domain-specific geological knowledge and difficulties in reasoning across multiple remote-sensing images, further exacerbating long-context issues. To address these, we present MineAgent, a modular framework leveraging hierarchical judging and decision-making modules to improve multi-image reasoning and spatial-spectral integration. Complementing this, we propose MineBench, a benchmark specific for evaluating MLLMs in domain-specific mineral exploration tasks using geological and hyperspectral data. Extensive experiments demonstrate the effectiveness of MineAgent, highlighting its potential to advance MLLMs in remote-sensing mineral exploration.

## 1 Introduction

Mineral exploration is a systematic geological investigation focused on locating, identifying, and evaluating economically viable mineral deposits (Dentith and Mudge, 2014). It is essential to discover and secure raw materials critical for global infrastructure, technological advancement, and sustainable development (Gocht et al., 2012). Nowadays, remote-sensing satellite imaging studies are widely and effectively used in mineral exploration, offering an efficient, cost-effective alternative to traditional field surveys (Van der Meer et al., 2012; Bedini, 2017; Ousmanou et al., 2024).

In remote-sensing mineral exploration, human experts typically follow: identifying *geological* features from images like faults and fractures, integrating multiple *hyperspectral* images to detect mineralization patterns, and synthesizing these into a mineral prospectivity map (MPM) to predict mineral deposit locations (Sabins, 1999; Shirmard

et al., 2022; Zuo et al., 2021). These processes are manual, time-intensive, and reliant on expert knowledge, necessitating automated machine learning and deep learning (DL) solutions for scalability.

To this end, DL models, e.g., CNNs (Alzubaidi et al., 2021; Fu et al., 2023) and Transformers (Yin et al., 2024a), have been widely applied to process remote-sensing (RS) data. These methods excel at extracting features from RS images, mapping geological, geochemical, and geophysical attributes to predict mineral deposits (Yang et al., 2024). However, their data-driven nature makes them reliant on labeled datasets, limiting their generalization to new geological scenarios. In contrast, multimodal large language models (MLLMs) have recently emerged with remarkable zero-shot capabilities, integrating visual and textual contexts to tackle tasks (Muhtar et al., 2024; Zhang et al., 2024c; Wang et al., 2024a) without requiring task-specific training data (Yin et al., 2024b).

Despite their promise, MLLMs face critical challenges when applied to mineral exploration with multiple RS images: they *lack domain-specific geological knowledge* (Zhang et al., 2024b) and *struggle to reason effectively across multiple images* (Liu et al., 2024b; Zhao et al., 2024). What’s worse, domain-specific instructions (e.g., thousands of tokens) and multi-image inputs (e.g., 9 images) exacerbate the challenge by long-context issues that hinder reasoning accuracy (Liu et al., 2024c). For example, Figure 1(a) highlights how MLLMs struggle with critical spatial elements like the strategic placement of low-value areas (blue). Besides, in Figure 1(b), MLLMs demonstrate significant difficulty in synthesizing spatial relationships across multiple geological contexts.

To circumvent the challenges of domain-specific knowledge integration and multi-image reasoning in mineral exploration, we propose MineAgent, a modular MLLM framework specifically designed to address these complexities (Figure 3).

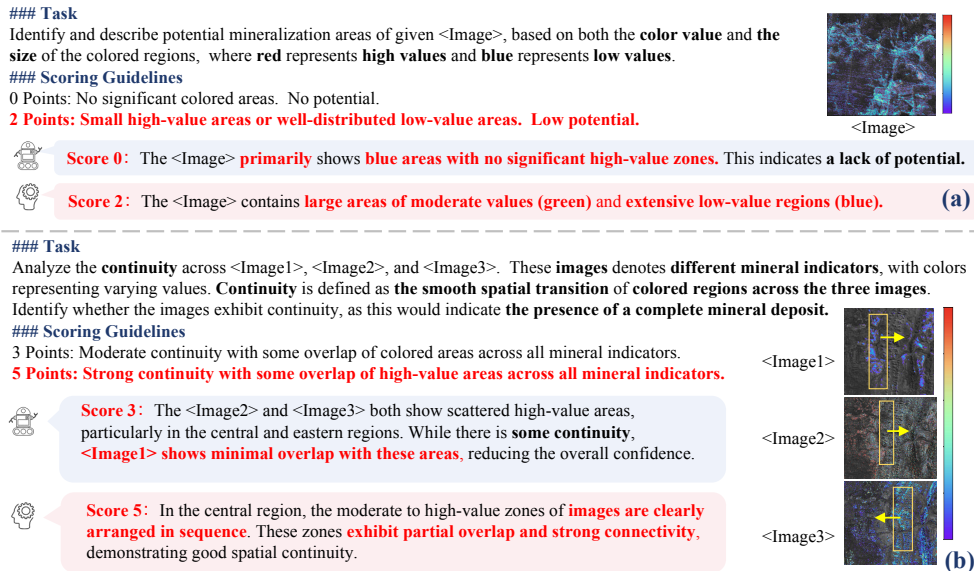


Figure 1: Judgment comparisons between GPT-4o (OpenAI, 2024) and human evaluator. GPT-4o in blue box and human-annotation in red box. In (b), yellow boxes highlight regions and their spatial relations identified by the human but not GPT-4o.

MineAgent employs hierarchical judging and decision-making modules to extract, integrate, and analyze spatial and spectral features from remote-sensing data. By considering the common-practice pipeline and orchestrating these modules, MineAgent enhances reasoning capabilities across geological and hyperspectral contexts, enabling accurate deposit predictions.

Moreover, we present MineBench, a benchmark for multimodal mineral exploration tasks. It standardizes task formulations and datasets, enabling rigorous evaluation of MLLMs in reasoning over domain-specific remote-sensing data. MineBench provides a unique challenge to MLLMs where both multi-image reasoning and long-tail domain understanding are required to accomplish one task. The main contributions of this work are:

- We propose MineAgent, a modular framework addressing domain challenges in multi-image reasoning for mineral exploration.
- We develop MineBench, a standardized benchmark for evaluating MLLMs in mineral exploration with geological and hyperspectral data.
- We conduct extensive experiments<sup>1</sup> across various models and setups, demonstrating MineAgent’s effectiveness and providing insights into MLLMs in this domain.

## 2 Related Work

**Multi-image Reasoning of MLLMs.** Recent studies have revealed a significant performance

<sup>1</sup>Our codes and data have been uploaded into the system.

gap between single- and multi-image reasoning tasks (Liu et al., 2024d; Wang et al., 2024b; Jiang et al., 2024; Zhang et al., 2024a; Liu et al., 2024b). For instance, Wang et al. (2024d) highlighted deficiencies in temporal and contextual reasoning across image sequences while Zhao et al. (2024) explored multi-dimensional aspects of multi-image reasoning, such as perception, knowledge integration, reasoning, and multi-hop inference. However, domain-specific tasks, such as those in mineral exploration, pose unique challenges requiring not only multi-image reasoning but also domain-specific knowledge. This motivates us to present MineBench to evaluate MLLMs’ reasoning capabilities within a long-tail domain rigorously.

**Remote Sensing MLLMs.** The application of MLLMs in remote sensing has gained traction for tasks like image captioning and visual question answering (Zhan et al., 2023; Cheng et al., 2022; Wang et al., 2021). These models, fine-tuned with extensive visual-text instructions, demonstrate strong performance on single-image tasks (Kuckreja et al., 2024; Zhan et al., 2024; Luo et al., 2024). However, their capabilities remain limited when extended to multi-image reasoning, a critical requirement for mineral exploration tasks that demand integration of spatial and spectral information across multiple images. Furthermore, the lack of standardized datasets tailored to multi-image remote-sensing tasks hinders progress in applying MLLMs to domains like mineral exploration. Addressing this gap, we propose a modular MLLM framework,

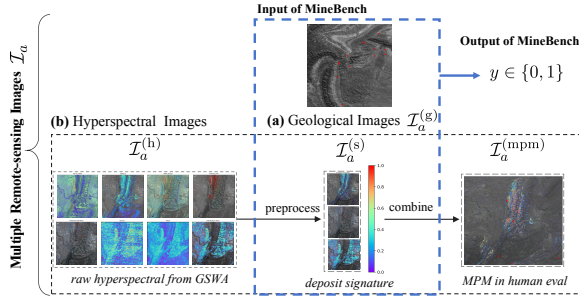


Figure 2: Task definition in MineBench. Particularly, a targeted area  $a$  is represented by two image types, i.e.,  $\mathcal{I}_a = \{\mathcal{I}_a^{(g)}, \mathcal{I}_a^{(h)}\}$ .  $\mathcal{I}_a^{(h)}$  are color-coded images where uncolored regions represent sub-threshold potential.

MineAgent, coupled with MineBench.

### 3 MineBench: on Remote-sensing Images

The field of mineral exploration currently lacks a well-organized benchmark to evaluate the performance of MLLMs. Existing ones do not capture the unique challenges of integrating geological knowledge with multimodal reasoning. These motivate us to present a new mineral exploration benchmark.

**Task Formulation.** Mineral exploration enables quantifiable assessments of deposit likelihood, facilitating prioritization of exploration areas, so it is usually formulated as a binary classification problem (Alzubaidi et al., 2021; Fu et al., 2023), i.e.,

$$y \sim P_\theta(y|a) := P_\theta(\cdot|\mathcal{I}_a) = P_\theta(\cdot|\mathcal{I}_a^{(g)}, \mathcal{I}_a^{(h)}) \quad (1)$$

where  $y \in \mathcal{Y}$  represents the presence of mineral deposits with  $\mathcal{Y} = \{0, 1\}$  in a targeted area  $a$  and  $a$  can be represented as a set of remote-sensing images,  $\mathcal{I}^a$ . In mineral exploration, according to distinct roles and nature of the data,  $\mathcal{I}^a$  can be coarsely grouped into two sub-sets, i.e., geological images ( $\mathcal{I}_a^{(g)}$ ) and hyperspectral images ( $\mathcal{I}_a^{(h)}$ ).

#### Remote-sensing Images in Mineral Exploration.

*Geological images* ( $\mathcal{I}_a^{(g)}$ ), see Figure 2(a) focus on capturing macroscopic spatial and morphological features, such as landforms, tectonic structures, and geological units, which are critical for identifying large-scale mineralization patterns and structural controls, whereas *hyperspectral images* ( $\mathcal{I}_a^{(h)}$ ), see Figure 2(b) are designed to capture high-resolution spectral reflectance data across a wide range of wavelengths, enabling the detailed characterization and differentiation of mineral types and their spatial distributions at a pixel-by-pixel level.

**Data Sourcing and Preprocessing.** We utilized raw remote-sensing data from the Geoscience Western Australia (GSWA) repository<sup>2</sup>, an open-source geoscience data source (Portal), to compose MineBench. Although the raw remote-sensing images encompass all necessary information to infer mineral exploration tasks, the raw hyperspectral images,  $\mathcal{I}_a^{(h)}$ , are not intuitive for visualizing mineralization patterns (Sabins, 1999). This limitation makes it considerably challenging for MLLMs or even humans to identify meaningful deposit signatures directly because such tasks require extensive domain knowledge in mineral exploration to interpret and process the raw data effectively. Therefore, following common practices in mineral exploration (Yazdi et al., 2018; Wambo et al., 2020; Ghamisi et al., 2017), we preprocess the raw hyperspectral images using domain-specific linear combinations to generate three distinct deposit signature images,  $\mathcal{I}_a^{(s)}$  (see Figure 2(bottom)). These signature images provide a visually interpretable representation of key features in deposit formation, significantly reducing task complexity for both human experts and automated models. Consequently, MineBench is formulated as

$$y \sim P_\theta(y|\mathcal{I}_a^{(g)}, \mathcal{I}_a^{(s)}). \quad (2)$$

More details on data sourcing and preprocessing are provided in Appendix A and B, respectively.

**Data Labeling and Sampling.** We access the deposit locations directly sourced from authoritative records as class labels<sup>3</sup> – ‘positive’ as  $y = 1$  and ‘negative’ as  $y = 0$ . Considering the inherent class imbalance in real-world mineral exploration, a strategic random sampling approach was employed to ensure robust evaluation close to real-world scenarios. The resulting dataset consists of 73 positive areas and 539 negative areas, yielding an  $\sim 1:9$  positive-to-negative ratio, leading to reliable and statistically meaningful evaluations (Hewson et al., 2015; Gonzalez-Alvarez et al., 2020).

**Validation of Preprocessing.** While preprocessing provides visually interpretable features for mineral exploration, it inherently involves a loss of information due to the linear combinations. To ensure that the processed data retains sufficient detail for deterministic judgments, we also conducted a

<sup>2</sup>[https://data.dea.ga.gov.au/?prefix=ASTER\\_Geoscience\\_Map\\_of\\_Australia/](https://data.dea.ga.gov.au/?prefix=ASTER_Geoscience_Map_of_Australia/)

<sup>3</sup><https://map.sarig.sa.gov.au/>

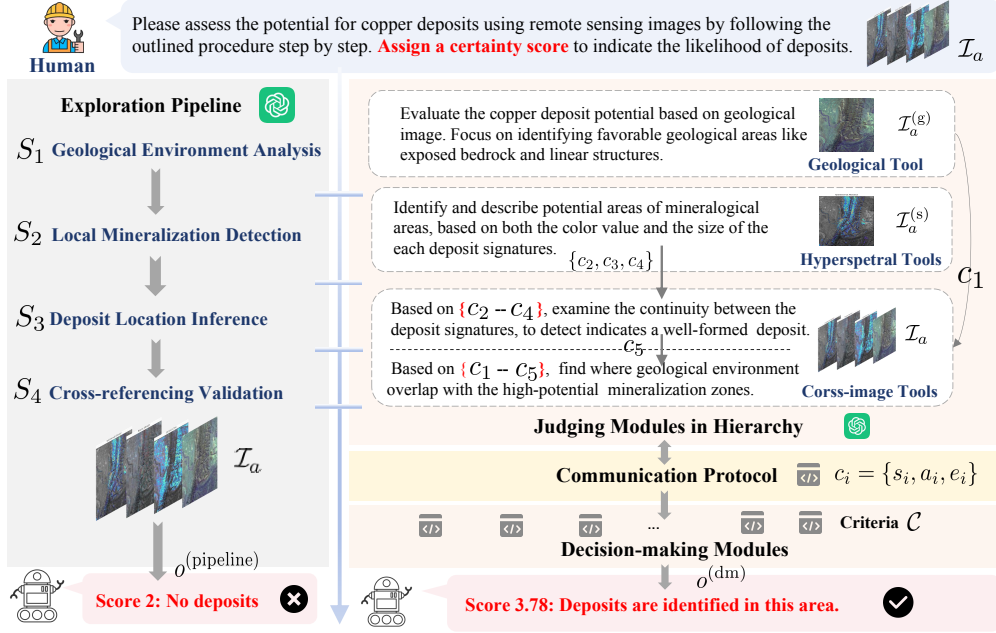


Figure 3: The tailored MineAgent for mineral exploration. (Left) Base pipeline using step-by-step reasoning; (Right) MineAgent decomposing pipeline into specialized modules, improving assessment accuracy.

human evaluation on a subset (20%) of the dataset. To facilitate this evaluation, the deposit signature images,  $\mathcal{I}_a^{(s)}$ , were further combined into a mineral prospectivity map (MPM),  $\mathcal{I}_a^{(\text{mpm})}$ , offering a clear and intuitive visualization of potential mineral deposits (Zuo, 2020; Xu et al., 2021). Using the MPM, human experts make judgments upon

$$\text{HumanEval}(\cdot | \mathcal{I}_a^{(g)}, \mathcal{I}_a^{(\text{mpm})}) \quad (3)$$

and validated the data by comparing it against official deposit locations. The results (97.4% accuracy) demonstrate that even with MPM, human judgments align well with the provided class labels, confirming the reliability of the preprocessing. Further details on the validation process are provided in Appendix B.4. In the remaining, we omit the subscript  $a$  for clarity if no confusion is caused.

## 4 Methodology

To leverage the capabilities of multimodal large language models (MLLMs) in mineral exploration, we naturally formulate the task as a visual question-answering (VQA) problem. Specifically, given remote-sensing images (e.g.,  $\mathcal{I}^{(g)}$  and  $\mathcal{I}^{(s)}$ ) and a domain-specific query about the presence of a particular mineral deposit, the model generates a response indicating the likelihood of the deposit. This response can then be mapped to a classifica-

tion label using a predefined verbalizer, i.e.,

$$o \sim \mathcal{M}(\mathcal{I}^{(g)}, \mathcal{I}^{(s)}; \theta), \quad (4)$$

where  $\theta$  parameterizes the MLLM,  $\mathcal{M}$ , and  $o$  denotes a natural language response with verbalizer.

Despite the simplicity in Eq.(4), the inherent limitations of MLLMs in lacking domain-specific geological knowledge pose significant challenges – they struggle with interpreting complex hyperspectral imaging data and understanding spatial patterns critical for mineral exploration.

### 4.1 Baseline: Mineral Exploration Pipeline

To alleviate the lack of domain knowledge, we first propose a baseline framework that integrates the conventional mineral exploration pipeline with domain-specific instructions to enhance the understanding and reasoning capabilities of MLLMs. This pipeline emulates the workflow of human experts in mineral exploration by leveraging step-by-step structured prompts and reasoning mechanisms.

Formally, let  $P$  denote a curated set of domain-specific prompts tailored for the task. These prompts are carefully designed to encode key domain knowledge and guide the MLLM through sequential reasoning steps. The method can be represented as

$$o^{(\text{pipeline})} \sim \mathcal{M}(\mathcal{I}^{(g)}, \mathcal{I}^{(s)}; \theta, P), \quad (5)$$

where  $\mathcal{I}^{(g)}$  and  $\mathcal{I}^{(s)}$  represent geological and processed hyperspectral images, and  $o^{(\text{pipeline})}$  is the model-generated step-by-step reasoning by following the pipeline instruction  $P$ .

Specifically, pipeline instruction  $P$  consists of sequential stages that transform raw geological data into actionable insights: *Geological Environment Analysis* ( $S_1$ ) analyzes geological images to identify key structural elements, such as faults, crucial for understanding the mineralization environment. *Local Mineralization Detection* ( $S_2$ ) uses hyperspectral images to detect deposit signatures by examining color variations, providing granular insights into potential mineralization zones. *Global Deposit Location Inference* ( $S_3$ ) evaluates spatial correlations among deposit signatures to infer deposit locations based on mineralization patterns. Sequential arrangements with strong spatial continuity suggest the presence of complete deposits. *Cross-referencing Validation* ( $S_4$ ) synthesizes findings from  $S_1$  to  $S_3$  to estimate deposit probabilities and accurately identify target exploration areas. Therefore,  $o^{(\text{pipeline})}$  can be decomposed as

$$o^{(\text{pipeline})} := o^{(s1)} \oplus o^{(s2)} \oplus o^{(s3)} \oplus o^{(s4)} \oplus y, \quad (6)$$

where  $o^{(s^*)}$  denotes the rationale and staged judgment generated for the corresponding stage, and  $y$  is the final judgment. Note we generate all outputs in  $o^{(\text{pipeline})}$  together in one MLLM inference (see Appendix H for details). As such, this structured pipeline enhances the reliability of mineral exploration by ensuring transparency at every stage.

## 4.2 MineAgent: Orchestrating over Remote-sensing Images

However, the above is still vulnerable to multi-image reasoning as MLLMs struggle to synthesize spatial and contextual relationships across multiple images and long contexts, leading to incomplete understandings of multiple remote-sensing images for mineral exploration. Therefore, we propose an agent framework, MineAgent, that decomposes the exploration process into modular components.

### 4.2.1 General MineAgent Framework

MineAgent focuses on two core kinds of modules to enhance its reasoning capabilities: *judging* and *decision-making*, as shown in Figure 4. While a judging module specializes in extracting specific features from remote-sensing images (e.g., geological structures or spectral mineralization signatures), a decision-making module is designed for

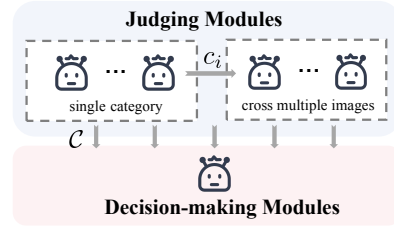


Figure 4: A general framework of MineAgent.

a specific task to integrate these features to perform high-level reasoning tasks, such as inferring mineral deposit likelihood or validating predictions across diverse datasets.

**Judging Modules in Hierarchy.** A judging module operates with two types of inputs to maintain focus and robustness in feature extraction, i.e.,

$$c \sim \mathcal{J}(\mathcal{I}, \mathcal{C}; \theta), \text{ where } \mathcal{C} = \{c_i\}_{i=0}^N. \quad (7)$$

The first type of input includes one or a few single-category remote-sensing images,  $\mathcal{I}$ , such as geological or hyperspectral images, ensuring that the module specializes in analyzing a specific feature (e.g., structural patterns or deposit signatures). The second type of input comes from the outputs,  $\mathcal{C}$ , of other judging modules, enabling a hierarchical structure. And either of them is optional. This setup allows for cross-image reasoning and intermediate result validation, effectively integrating insights from multiple sources. By focusing on specific features while facilitating inter-module communication, this approach circumvents the challenges of multi-image reasoning in complex mineral exploration tasks.

**Communication Protocol.** A well-defined communication protocol is critical for ensuring efficient information exchange between modules. Each module in MineAgent communicates using a semi-structured output format,

$$c_i = \{s_i, a_i, e_i\}, \quad (8)$$

where  $s_i$  is a numerical score reflecting the module’s confidence or evaluation,  $a_i$  represents the identified favorable areas or features, and  $e_i$  provides an analytical explanation or rationale behind the module’s output.  $s_i$  is determined based on a detailed scoring guide, ensuring consistency.

**Decision-making Modules Specific to Tasks.**

A decision-making module is invoked to integrate

| Tool Type             | Module Type     | Captured Feature   | Inp. Imgs ( $\mathcal{I}$ )                | Inp. Ref ( $\mathcal{C}$ ) | Output     | Stage |
|-----------------------|-----------------|--|--|----------------------------|------------|-------|
| Geological Tool       | Judging         | Geological context   | $\mathcal{I}_a^{(g)}$                      | N/A                        | $c_1$      | $S_1$ |
|                       | Judging         | Signature 1  | $\mathcal{I}^{(s)}$                        | N/A                        | $c_2$      | $S_2$ |
| Hyperspectral Tools   | Judging         | Signature 2  | $\mathcal{I}_a^{(g)}$                      | N/A                        | $c_3$      | $S_2$ |
|                       | Judging         | Signature 3  | $\mathcal{I}_a^{(s)}$                      | N/A                        | $c_4$      | $S_2$ |
| Corss-image Tools     | Judging         | Relation between signatures  | $\mathcal{I}^{(s)}$                        | $c_2-c_4$                  | $c_5$      | $S_3$ |
|                       | Judging         | Validation between $\mathcal{I}_a^{(g)}$ and $\mathcal{I}_a^{(s)}$ | $\mathcal{I}_a^{(g)}, \mathcal{I}_a^{(s)}$ | $c_1-c_5$                  | $c_6$      | $S_4$ |
| Deposit Presence Tool | Decision-making | Response of deposit presence                                       | N/A  | N/A                        | $o^{(dm)}$ | N/A   |

Table 1: Tools in MineAgent tailored for mineral exploration. ‘Inp.’ denotes the model inputs in Eq.(7).

multiple structured outputs from the judging modules to derive high-level insights and outputs for a specific task. Formally, this task-specific module is written as

$$o^{(dm)} := \mathcal{D}(\mathcal{C}; \theta), \quad (9)$$

The module takes a set of assessment tuples  $\mathcal{C} = \{c_1, c_2, \dots, c_M\}$  as input and outputs  $o^{(dm)}$ , the final decision, along with a confidence score or feedback to guide downstream processes.

Thus, MineAgent orchestrates the exploration process by integrating judgments from hierarchical judging modules and decisions from task-specific decision-making modules, ensuring robust multi-image reasoning and high-confidence answers.

#### 4.2.2 Grounding for Mineral Exploration

As we have a mature pipeline for mineral exploration with remote-sensing images according to human experts, we apply a workflow-based paradigm (Li et al., 2024) to our agent framework for mineral exploration.

To ground the MineAgent, we propose multiple tools as in Table 1 for judging modules in Eq.(7) and decision-making modules in Eq.(9): *remote-sensing image judging tool* suite is a collection of MLLM-based modules designed to extract critical features from remote-sensing data, including geological and hyperspectral images (see Appendix H for details). And *deposit presence decision-making tool* insights from the judging modules to determine the likelihood of mineral deposit presence in a targeted area. To optimize computational efficiency, we directly employ Bayesian optimization (Snoek et al., 2012) to calculate the overall evaluation score  $o^{(dm)} = \sum w_i s_i$ , where  $w_i$  represents the weight assigned to each criterion.

## 5 Experiment

**Metric.** Due to the inherent class imbalance in MineBench, multiple complementary metrics

are employed. The F1 score for positive classes (Pos.F1) evaluates the MLLMs’ ability to identify deposits. The macro-averaged F1 score (Avg.F1) provides balanced assessment across classes, while the Roc-AUC evaluates discriminative ability. Additionally, the Matthews Correlation Coefficient (MCC) provides a comprehensive evaluation by synthesizing the confusion matrix ranging from -1 to 1, where -1 indicates complete misclassification, 1 represents perfect prediction (Chicco and Jurman, 2020). The details of the experimental setting are provided in Appendix C.

### 5.1 Main Results

Table 2 presents the comparative performance of various MLLMs: Qwen2-VL-7B/72B (Bai et al., 2023; Wang et al., 2024c), Gemini-Flash-2.0 (Team et al., 2024), Gemini-Pro-1.5, GPT- 4o (OpenAI, 2024), LLaVA-13B (Liu et al., 2023b, 2024a), Yi-6B/34B (Young et al., 2024) and InterVL-26B (Chen et al., 2024) on MineBench. This evaluation highlights several key findings regarding the strengths and limitations of the MLLMs:

**Effectiveness of MineAgent.** Experimental results demonstrate significant performance improvements achieved by MineAgent, with the highest improvement reaching 30.14% when paired with GPT-4o and 23.77% when paired with Qwen-7B. This result highlights the potential of MineAgent in enhancing multi-image reasoning and domain-specific gaps. Few open-source MLLMs, especially smaller ones (e.g., Yi-6B and LLaVA-13B), show performance degradation when integrated with MineAgent, primarily due to their unstable reasoning capabilities in interpreting score criteria. This problem, existing in both baseline and MineAgent, leads to a label-score mismatch problem, such as assigning a score of 5 as “positive” and a score of 9 as “negative.”, making the outputs less meaningful. Statistically, Yi-6B exhibited a 23.53% label-score mismatch, while LLaVA-13B showed

| Source        | Model            | Baseline |        |         |       | with MineAgent |                |                |                |
|---------------|------------------|----------|--------|---------|-------|----------------|----------------|----------------|----------------|
|               |                  | Pos.F1   | Avg.F1 | Roc-AUC | MCC   | Pos.F1         | Avg.F1         | Roc-AUC        | MCC            |
| N/A           | Random Choice    | 11.86    | 49.96  | 51.01   | 2.01  | 11.86          | 49.96          | 51.01          | 2.01           |
| Closed-Source | Gemini-Pro-1.5   | 20.95    | 18.56  | 49.66   | -0.77 | 21.72 (+0.77)  | 30.57 (+12.01) | 52.34 (+2.68)  | 3.52 (+4.29)   |
|               | Gemini-Flash-2.0 | 20.30    | 41.24  | 51.33   | 1.73  | 22.54 (+2.24)  | 56.18 (+14.49) | 56.03 (+4.70)  | 12.37 (+10.6)  |
|               | Qwen2-VL-72B     | 22.97    | 20.76  | 54.44   | 9.97  | 58.71 (+34.74) | 75.30 (+54.54) | 84.01 (+29.6)  | 54.21 (+41.84) |
|               | GPT-4o           | 34.93    | 57.27  | 69.35   | 26.16 | 61.20 (+26.27) | 77.19 (+19.92) | 83.35 (+13.82) | 56.30 (+30.14) |
| Open-Source   | Yi-6B            | 15.74    | 43.89  | 47.14   | -3.82 | 21.82 (+6.08)  | 15.16 (-28.74) | 51.54 (+7.65)  | 5.05 (+8.87)   |
|               | LLaVA-13B        | 19.46    | 26.32  | 47.28   | -4.31 | 20.58 (+1.9)   | 21.36 (-4.96)  | 50.77(+3.49)   | 1.60 (+5.91)   |
|               | InterVL-26B      | 19.26    | 31.87  | 56.91   | 8.95  | 24.23 (+5.06)  | 44.32 (+12.45) | 57.10 (+0.19)  | 9.24 (+0.29)   |
|               | Yi-34B           | 22.16    | 43.63  | 54.28   | 5.55  | 29.71 (+7.10)  | 50.85 (+7.22)  | 64.82 (+10.34) | 19.28 (+13.73) |
|               | Qwen-7B          | 22.92    | 24.16  | 54.59   | 8.69  | 30.99 (+8.07)  | 47.93(+23.77)  | 68.23 (+13.64) | 23.79 (+15.10) |

Table 2: Comparison between baseline and MineAgent. Highlighted rows indicate the highest scores in either closed- or open-source MLLMs. Red denotes improvements from baseline, while Gray denotes the number worse than the random choice.

an even higher rate of 35.15%, compared to mere 1.96% for GPT-4o. Moreover, we observe a notable discrepancy between scores and their corresponding explanations from smaller MLLMs, as detailed in Appendix D. These findings underscore the critical importance of stable foundational models in achieving consistent performance improvements.

**Performance Ceiling.** MLLMs encounter significant limitations when addressing mineral exploration tasks, even with the enhanced reasoning capabilities provided by MineAgent. For instance, GPT-4o achieves a Pos.F1 score of only 61.21% and an Avg.F1 of 77.19%. Notably, several open-source MLLMs perform below the random choice, underscoring fundamental architectural constraints. Moreover, a substantial performance disparity exists between closed-source and open-source MLLMs. This performance gap stems from two factors: a lack of high-quality, domain-specific training data to capture the nuances and insufficient exposure to multi-image reasoning scenarios needed for handling task complexity.

## 5.2 MLLM Capabilities Evaluation

To assess MLLMs across varying levels of analytical complexity, we introduce a three-tiered evaluation framework. The most challenging “Hard”

setting employs raw remote-sensing data  $\mathcal{I}_a^{(h)}$ , from GSWA without preprocessing steps. This configuration rigorously tests MLLMs’ fundamental reasoning capabilities, demanding comprehensive interpretation with minimal prior knowledge. In the “Standard” setting, MineBench preprocesses  $\mathcal{I}_a^{(h)}$  into deposit signatures  $\mathcal{I}_a^{(s)}$ , exposing intuitive mineralization patterns. The “Easy” setting, further simplify the “Standard” MineBench by using a manually preprocessed mineral prospectivity map  $\mathcal{I}_a^{(mpm)}$ , incorporating extensive prior geological knowledge. MineBench statistics and task configurations are summarized in Table 3.

Experimental results reveal a clear correlation between task complexity and MLLM performance, as shown in Figure 5. As settings demand more sophisticated domain expertise and multi-image reasoning, performance metrics systematically decline. Even the state-of-the-art GPT-4o demonstrates this trend, with Avg.F1 scores declining from 87.41% in the “Easy” task to 60.47% in the “Hard” task. These findings underscore MineBench’s critical role in identifying and facilitating improvements to current MLLM limitations by offering diverse, strategically designed evaluation settings.

## 5.3 Alignment of MLLMs with Human

Following scoring guidelines, both the human expert and the MLLM are tasked with assigning a score within defined areas to evaluate reasoning ability in this evaluation. The evaluation employed 20% of the MineBench, with samples selected randomly while maintaining the original positive-negative class distribution. The quantitative results (Figure 6) reveal two key findings:

| Setting  | Input  |        | Output     |
|----------|--|--------|------------|
|          | Inp.Imags ( $\mathcal{I}$ )                  | Number |            |
| Easy     | $\mathcal{I}_a^{(g)}, \mathcal{I}_a^{(mpm)}$ | 2      | $o^{(dm)}$ |
| Standard | $\mathcal{I}_a^{(g)}, \mathcal{I}_a^{(s)}$   | 4      | $o^{(dm)}$ |
| Hard     | $\mathcal{I}_a^{(g)}, \mathcal{I}_a^{(h)}$   | 9      | $o^{(dm)}$ |

Table 3: Statistics of various settings.

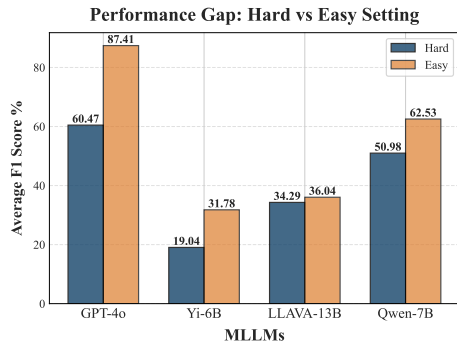


Figure 5: Performance across varying complexity levels

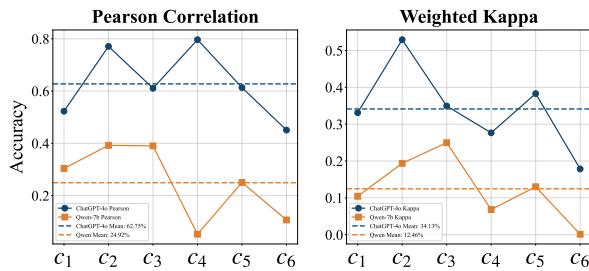


Figure 6: comparison of MLLMs and human assessment w.r.t Pearson correlation and weighted kappa across six outputs ( $c_1$  to  $c_6$ ). The dashed lines indicate avg. performance.

**Model-Human Alignment.** GPT-4o demonstrated significantly higher Pearson correlation and weighted Kappa scores than Qwen-7B across all evaluation criteria. This strong alignment with human expert correlates with the models’ overall performance, validating that higher-performing MLLMs can better approximate human scoring patterns (Ouyang et al., 2022). To provide a comprehensive view of the models’ scoring patterns, we visualize the score distributions in Appendix E.

**Challenges in Complex Task.** The output  $c_6$  exhibited the lowest consistency scores, falling well below the average. This result underscores a key limitation: even advanced methods face difficulties extracting features from multi-image reasoning, which emphasizes the current shortcomings of MLLMs in handling mineral exploration tasks.

## 5.4 Ablation Studies

We conducted ablation studies to evaluate the effectiveness of MineAgent by analyzing its components using GPT-4o. Four variants were designed and evaluated to investigate the role of each component in handling tasks of different complexity levels. 1) *MineAgent*: The framework incorporates all components, including the judging modules, communication protocol, and decision-making modules.

| Setting  | Component | Pos.F1       | Avg.F1       | Roc-Auc      | Mcc          |
|----------|-----------|--------------|--------------|--------------|--------------|
| Standard | MineAgent | <b>61.20</b> | <b>77.19</b> | <b>83.35</b> | <b>56.30</b> |
|          | w/o J     | 54.73        | 72.92        | 80.90        | 49.25        |
|          | w/o JC    | 32.51        | 59.05        | 82.28        | 34.94        |
|          | BASE      | 34.93        | 57.27        | 69.35        | 26.16        |
| Easy     | MineAgent | 71.62        | 83.86        | 84.26        | 67.73        |
|          | w/o A     | 44.00        | 62.91        | 80.27        | 40.62        |
|          | w/o JC    | <b>77.78</b> | <b>87.41</b> | <b>86.96</b> | <b>74.82</b> |
|          | BASE      | 55.24        | 75.52        | 69.58        | 57.03        |

Table 4: Performance across different settings and components. The highest scores are marked in bold.

2) *w/o J*: A variant of MineAgent that removes the judging modules, implementing the exploration pipeline in a single inference. 3) *w/o JC*: Extending *w/o J*, this version further excludes the communication protocol, resulting in the absence of detailed scoring guidelines. 4) *BASE*: A simplified version that additionally excludes the decision-making module, producing  $o^{(\text{pipeline})}$  as the result.

The results show MineAgent effectively reduces reasoning complexity by decomposing the pipeline into manageable components: The removal of judging modules led to a 7.05% decline in the MCC score. Excluding the detailed scoring guidelines within the communication protocol caused a substantial performance drop. Further, the decision-making modules played a critical role in enhancing the MLLM’s capability to navigate the exploration pipeline. The details of the decision-making modules are further analyzed in Appendix F, showing their effectiveness. In the “Easy” setting, an unexpected performance pattern emerged: the *w/o JC* variant outperformed the full MineAgent framework. This result aligns with prior findings: while existing MLLMs excel in basic visual reasoning, they often struggle with complex multi-image and domain-specific tasks (Kazemi et al., 2024).

## 6 Conclusion

In this paper, we present MineAgent, a novel MLLM agent framework designed to address critical challenges in multi-image reasoning and domain-specific gap for mineral exploration. Our comprehensive quantitative and qualitative ablation studies further validate the effectiveness of MineAgent. Further, our results underscore both the potential and the limitations of MLLMs in mineral exploration, revealing significant performance degradation as task complexity increases.

## 562 Limitation

563 1) *Generalized applications*: This work can only  
564 recognize specific types of deposits, restricting its  
565 applicability to a wider range of mineral types. 2)  
566 *Domain-Specific Knowledge Enhancement*: Con-  
567 tinuing from the initial success of MineAgent, fu-  
568 ture work will explore strategies such as integrat-  
569 ing domain-specific knowledge bases or leverag-  
570 ing reinforcement learning to further improve the  
571 MLLMs' performance in specialized tasks. 3) *As-*  
572 *istant Tools* : The results under the "Hard" setting  
573 highlight significant challenges. Future research  
574 will integrate assistant tools, such as integrating  
575 coding agents or feedback loops, can enhance the  
576 robustness and reasoning capabilities of models in  
577 realistic environments.

## 578 References

579 Fatimah Alzubaidi, Peyman Mostaghimi, Pawel Swieto-  
580 janski, Stuart R Clark, and Ryan T Armstrong. 2021.  
581 Automated lithology classification from drill core im-  
582 ages using convolutional neural networks. *Journal of*  
583 *Petroleum Science and Engineering*, 197:107933.

584 Jinze Bai, Shuai Bai, Shusheng Yang, Shijie Wang,  
585 Sinan Tan, Peng Wang, Junyang Lin, Chang Zhou,  
586 and Jingren Zhou. 2023. Qwen-vl: A versatile  
587 vision-language model for understanding, localiza-  
588 tion, text reading, and beyond. *arXiv preprint*  
589 *arXiv:2308.12966*.

590 Enton Bedini. 2017. The use of hyperspectral remote  
591 sensing for mineral exploration: A review. *Journal*  
592 *of Hyperspectral Remote Sensing*, 7(4):189–211.

593 Emmanuel John Muico Carranza. 2008. *Geochemical*  
594 *anomaly and mineral prospectivity mapping in GIS*.  
595 Elsevier.

596 Zhe Chen, Jiannan Wu, Wenhai Wang, Weijie Su, Guo  
597 Chen, Sen Xing, Muyan Zhong, Qinglong Zhang,  
598 Xizhou Zhu, Lewei Lu, et al. 2024. Internvl: Scal-  
599 ing up vision foundation models and aligning for  
600 generic visual-linguistic tasks. In *Proceedings of*  
601 *the IEEE/CVF Conference on Computer Vision and*  
602 *Pattern Recognition*, pages 24185–24198.

603 Qimin Cheng, Haiyan Huang, Yuan Xu, Yuzhuo Zhou,  
604 Huanying Li, and Zhongyuan Wang. 2022. Nwpu-  
605 captions dataset and mlca-net for remote sensing im-  
606 age captioning. *IEEE Transactions on Geoscience*  
607 *and Remote Sensing*, 60:1–19.

608 Davide Chicco and Giuseppe Jurman. 2020. The advan-  
609 tages of the matthews correlation coefficient (mcc)  
610 over f1 score and accuracy in binary classification  
611 evaluation. *BMC genomics*, 21:1–13.

Michael Dentith and Stephen T Mudge. 2014. *Geo-*  
*physics for the mineral exploration geoscientist*.  
Cambridge University Press.

Xuefeng Du, Chaowei Xiao, and Yixuan Li. 2024.  
Haloscope: Harnessing unlabeled llm genera-  
tions for hallucination detection. *arXiv preprint*  
*arXiv:2409.17504*.

Yufeng Fu, Qiuming Cheng, Linhai Jing, Bei Ye, and  
Hanze Fu. 2023. Mineral prospectivity mapping of  
porphyry copper deposits based on remote sensing  
imagery and geochemical data in the duolong ore  
district, tibet. *Remote Sensing*, 15(2):439.

Pedram Ghamisi, Naoto Yokoya, Jun Li, Wenzhi Liao,  
Sicong Liu, Javier Plaza, Behnood Rasti, and Anto-  
nio Plaza. 2017. Advances in hyperspectral image  
and signal processing: A comprehensive overview  
of the state of the art. *IEEE Geoscience and Remote*  
*Sensing Magazine*, 5(4):37–78.

Werner R Gocht, Half Zantop, and Roderick G Eggert.  
2012. *International mineral economics: mineral ex-*  
*ploration, mine valuation, mineral markets, interna-*  
*tional mineral policies*. Springer Science & Business  
Media.

Ignacio Gonzalez-Alvarez, MA Goncalves, and Em-  
manuel John M Carranza. 2020. Introduction to the  
special issue challenges for mineral exploration in  
the 21st century: Targeting mineral deposits under  
cover. *Ore Geology Reviews*, 126:103785.

Robert Hewson, D Robson, Alan Mauger, Thomas Cud-  
ahy, Matilda Thomas, and Simon Jones. 2015. Using  
the geoscience australia-csiro aster maps and airborne  
geophysics to explore australian geoscience. *Journal*  
*of Spatial Science*, 60(2):207–231.

Dongfu Jiang, Xuan He, Huaye Zeng, Cong Wei, Max  
Ku, Qian Liu, and Wenhui Chen. 2024. Mantis: Inter-  
leaved multi-image instruction tuning. *arXiv preprint*  
*arXiv:2405.01483*.

Mehran Kazemi, Nishanth Dikkala, Ankit Anand, Petar  
Devic, Ishita Dasgupta, Fangyu Liu, Bahare Fatemi,  
Pranjal Awasthi, Dee Guo, Sreenivas Gollapudi, et al.  
2024. Remi: A dataset for reasoning with multiple  
images. *arXiv preprint arXiv:2406.09175*.

Kartik Kuckreja, Muhammad Sohail Danish, Muza-  
mmal Naseer, Abhijit Das, Salman Khan, and Fa-  
had Shahbaz Khan. 2024. Geochat: Grounded large  
vision-language model for remote sensing. In *Pro-*  
*ceedings of the IEEE/CVF Conference on Computer*  
*Vision and Pattern Recognition*, pages 27831–27840.

Zelong Li, Shuyuan Xu, Kai Mei, Wenyue Hua, Bal-  
aji Rama, Om Raheja, Hao Wang, He Zhu, and  
Yongfeng Zhang. 2024. Autoflow: Automated work-  
flow generation for large language model agents.  
*arXiv preprint arXiv:2407.12821*.

|     |  |  |     |
|-----|--|--|-----|
| 665 | Cai Liu, Wenlei Wang, Juxing Tang, Qin Wang,                                     | Binh Thai Pham, Indra Prakash, and Dieu Tien Bui.            | 720 |
| 666 | Ke Zheng, Yanyun Sun, Jiahong Zhang, Fuping Gan,                                 | 2018. Spatial prediction of landslides using a hy-           | 721 |
| 667 | and Baobao Cao. 2023a. A deep-learning-based min-                                | brid machine learning approach based on random               | 722 |
| 668 | eral prospectivity modeling framework and workflow                               | subspace and classification and regression trees. <i>Ge-</i> | 723 |
| 669 | in prediction of porphyry–epithermal mineralization                              | <i>omorphology</i> , 303:256–270.                            | 724 |
| 670 | in the duolong ore district, tibet. <i>Ore Geology Re-</i>                       |  |     |
| 671 | <i>views</i> , 157:105419.   |  |     |
| 672 | Haotian Liu, Chunyuan Li, Yuheng Li, Bo Li, Yuanhan                              | AuScope Discovery Portal. Satellite aster geoscience         | 725 |
| 673 | Zhang, Sheng Shen, and Yong Jae Lee. 2024a. Llava-                               | product notes for australia.                                 | 726 |
| 674 | next: Improved reasoning, ocr, and world knowledge.                              |  |     |
| 675 | Haotian Liu, Chunyuan Li, Qingyang Wu, and Yong Jae                              | Zhongliang Ren, Lin Sun, and Qiuping Zhai. 2020. Im-         | 727 |
| 676 | Lee. 2023b. Visual instruction tuning.   | proved k-means and spectral matching for hyper-              | 728 |
|     |  | spectral mineral mapping. <i>International Journal</i>       | 729 |
| 677 | Haowei Liu, Xi Zhang, Haiyang Xu, Yaya Shi, Chaoya                               | <i>of Applied Earth Observation and Geoinformation</i> ,     | 730 |
| 678 | Jiang, Ming Yan, Ji Zhang, Fei Huang, Chunfeng                                   | 91:102154.   | 731 |
| 679 | Yuan, Bing Li, et al. 2024b. Mibench: Evaluating                                 |  |     |
| 680 | multimodal large language models over multiple im-                               | Floyd F Sabins. 1999. Remote sensing for mineral             | 732 |
| 681 | ages. <i>arXiv preprint arXiv:2407.15272</i> .                                   | exploration. <i>Ore geology reviews</i> , 14(3-4):157–183.   | 733 |
| 682 | Nelson F Liu, Kevin Lin, John Hewitt, Ashwin Paran-                              |  |     |
| 683 | jape, Michele Bevilacqua, Fabio Petroni, and Percy                               | Hojat Shirmard, Ehsan Farahbakhsh, R Dietmar Müller,         | 734 |
| 684 | Liang. 2024c. Lost in the middle: How language                                   | and Rohitash Chandra. 2022. A review of machine              | 735 |
| 685 | models use long contexts. <i>Transactions of the Asso-</i>                       | learning in processing remote sensing data for min-          | 736 |
| 686 | <i>ciation for Computational Linguistics</i> , 12:157–173.                       | eral exploration. <i>Remote Sensing of Environment</i> ,     | 737 |
|     |  | 268:112750.  | 738 |
| 687 | Ziyu Liu, Tao Chu, Yuhang Zang, Xilin Wei, Xiaoyi                                | Jasper Snoek, Hugo Larochelle, and Ryan P Adams.             | 739 |
| 688 | Dong, Pan Zhang, Zijian Liang, Yuanjun Xiong,                                    | 2012. Practical bayesian optimization of machine             | 740 |
| 689 | Yu Qiao, Dahua Lin, et al. 2024d. Mmdu: A  | learning algorithms. <i>Advances in neural information</i>   | 741 |
| 690 | multi-turn multi-image dialog understanding bench-                               | <i>processing systems</i> , 25.                              | 742 |
| 691 | mark and instruction-tuning dataset for lvlms. <i>arXiv</i>                      |  |     |
| 692 | <i>preprint arXiv:2406.11833</i> .   | Gemini Team, Petko Georgiev, Ving Ian Lei, Ryan              | 743 |
| 693 | Junwei Luo, Zhen Pang, Yongjun Zhang, Tingzhu Wang,                              | Burnell, Libin Bai, Anmol Gulati, Garrett Tanzer,            | 744 |
| 694 | Linlin Wang, Bo Dang, Jiangwei Lao, Jian Wang,                                   | Damien Vincent, Zhufeng Pan, Shibo Wang, et al.              | 745 |
| 695 | Jingdong Chen, Yihua Tan, et al. 2024. Skysensegpt:                              | 2024. Gemini 1.5: Unlocking multimodal under-                | 746 |
| 696 | A fine-grained instruction tuning dataset and model                              | standing across millions of tokens of context. <i>arXiv</i>  | 747 |
| 697 | for remote sensing vision-language understanding.                                | <i>preprint arXiv:2403.05530</i> .                           | 748 |
| 698 | <i>arXiv preprint arXiv:2406.10100</i> .   | Laurens Van der Maaten and Geoffrey Hinton. 2008.            | 749 |
| 699 | Dilxat Muhtar, Zhenshi Li, Feng Gu, Xueliang Zhang,                              | Visualizing data using t-sne. <i>Journal of machine</i>      | 750 |
| 700 | and Pengfeng Xiao. 2024. Lhrs-bot: Empowering                                    | <i>learning research</i> , 9(11).                            | 751 |
| 701 | remote sensing with vgi-enhanced large multimodal                                |  |     |
| 702 | language model. <i>arXiv preprint arXiv:2402.02544</i> .                         | Freek D Van der Meer, Harald MA Van der Werff,               | 752 |
| 703 | OpenAI. 2024. Chatgpt-4o. Available at <a href="https://openai.com">https://</a> | Frank JA Van Ruitenbeek, Chris A Hecker, Wim H               | 753 |
| 704 | <a href="https://openai.com">openai.com</a> .                                    | Bakker, Marleen F Noomen, Mark Van Der Meijde,               | 754 |
| 705 | Safianou Ousmanou, Fozing Eric Martial, Tcheume-                                 | E John M Carranza, J Boudewijn De Smeth, and Tse-            | 755 |
| 706 | nak Kouémo Jules, Achu Megnemo Ludovic, Kam-                                     | shaie Woldai. 2012. Multi-and hyperspectral geologic         | 756 |
| 707 | gang Tchuifong Agnès Blandine, Aman Sufinatu,                                    | remote sensing: A review. <i>International journal</i>       | 757 |
| 708 | Rachid Mohamed, and Kwékam Maurice. 2024.  | <i>of applied Earth observation and geoinformation</i> ,     | 758 |
| 709 | Mapping and discrimination of the mineralization                                 | 14(1):112–128.   | 759 |
| 710 | potential in granitoids from banyo area (adamawa,                                | Jonas Didero Takodjou Wambo, Amin Beiranvand Pour,           | 760 |
| 711 | cameroon), using landsat 9 oli, aster images and                                 | Sylvestre Ganno, Paul D Asimow, Basem Zoheir,                | 761 |
| 712 | field observations. <i>Geosystems and Geoenvironment</i> ,                       | Rodrigo dos Reis Salles, Jean Paul Nzenti, Biswa-            | 762 |
| 713 | 3(1):100239.   | jeet Pradhan, and Aidy M Muslim. 2020. Identifying           | 763 |
| 714 | Long Ouyang, Jeffrey Wu, Xu Jiang, Diogo Almeida,                                | high potential zones of gold mineralization in a             | 764 |
| 715 | Carroll Wainwright, Pamela Mishkin, Chong Zhang,                                 | sub-tropical region using landsat-8 and aster remote         | 765 |
| 716 | Sandhini Agarwal, Katarina Slama, Alex Ray, et al.                               | sensing data: a case study of the ngoura-colomines           | 766 |
| 717 | 2022. Training language models to follow instruc-                                | goldfield, eastern cameroon. <i>Ore Geology Reviews</i> ,    | 767 |
| 718 | tions with human feedback. <i>Advances in neural in-</i>                         | 122:103530.  | 768 |
| 719 | <i>formation processing systems</i> , 35:27730–27744.                            | Di Wang, Jing Zhang, Bo Du, Minqiang Xu, Lin Liu,            | 769 |
|     |  | Dacheng Tao, and Liangpei Zhang. 2024a. Samrs:               | 770 |
|     |  | Scaling-up remote sensing segmentation dataset with          | 771 |
|     |  | segment anything model. <i>Advances in Neural Infor-</i>     | 772 |
|     |  | <i>mation Processing Systems</i> , 36.                       | 773 |

|     |   |  |     |
|-----|---|--|-----|
| 774 | Fei Wang, Xingyu Fu, James Y Huang, Zekun Li, Qin Liu, Xiaogeng Liu, Mingyu Derek Ma, Nan Xu, Wenxuan Zhou, Kai Zhang, et al. 2024b. Muirbench: A comprehensive benchmark for robust multi-image understanding. <i>arXiv preprint arXiv:2406.09411</i> .  |  |     |
| 775 |   |  |     |
| 776 |   |  |     |
| 777 |   |  |     |
| 778 |   |  |     |
| 779 | Junjue Wang, Zhuo Zheng, Ailong Ma, Xiaoyan Lu, and Yanfei Zhong. 2021. Loveda: A remote sensing land-cover dataset for domain adaptive semantic segmentation. <i>arXiv preprint arXiv:2110.08733</i> .   |  |     |
| 780 |   |  |     |
| 781 |   |  |     |
| 782 |   |  |     |
| 783 | Peng Wang, Shuai Bai, Sinan Tan, Shijie Wang, Zhihao Fan, Jinze Bai, Keqin Chen, Xuejing Liu, Jialin Wang, Wenbin Ge, Yang Fan, Kai Dang, Mengfei Du, Xuancheng Ren, Rui Men, Dayiheng Liu, Chang Zhou, Jingren Zhou, and Junyang Lin. 2024c. Qwen2-vl: Enhancing vision-language model's perception of the world at any resolution. <i>arXiv preprint arXiv:2409.12191</i> . |  |     |
| 784 |   |  |     |
| 785 |   |  |     |
| 786 |   |  |     |
| 787 |   |  |     |
| 788 |   |  |     |
| 789 |   |  |     |
| 790 |   |  |     |
| 791 | Xiyao Wang, Yuhang Zhou, Xiaoyu Liu, Hongjin Lu, Yuancheng Xu, Feihong He, Jaehong Yoon, Taixi Lu, Gedas Bertasius, Mohit Bansal, et al. 2024d. Mementos: A comprehensive benchmark for multimodal large language model reasoning over image sequences. <i>arXiv preprint arXiv:2401.10529</i> .  |  |     |
| 792 |   |  |     |
| 793 |   |  |     |
| 794 |   |  |     |
| 795 |   |  |     |
| 796 |   |  |     |
| 797 | Yongyang Xu, Zixuan Li, Zhong Xie, Huihui Cai, Pengfei Niu, and Hui Liu. 2021. Mineral prospectivity mapping by deep learning method in yawan-daqiao area, gansu. <i>Ore Geology Reviews</i> , 138:104316.  |  |     |
| 798 |   |  |     |
| 799 |   |  |     |
| 800 |   |  |     |
| 801 |   |  |     |
| 802 | Fanfan Yang, Renguang Zuo, and Oliver P Kreuzer. 2024. Artificial intelligence for mineral exploration: A review and perspectives on future directions from data science. <i>Earth-Science Reviews</i> , page 104941.   |  |     |
| 803 |   |  |     |
| 804 |   |  |     |
| 805 |   |  |     |
| 806 | Zahra Yazdi, Alireza Jafari Rad, Mehraj Aghazadeh, and Peyman Afzal. 2018. Alteration mapping for porphyry copper exploration using aster and quickbird multispectral images, sonajeel prospect, nw iran. <i>Journal of the Indian Society of Remote Sensing</i> , 46:1581–1593.  |  |     |
| 807 |   |  |     |
| 808 |   |  |     |
| 809 |   |  |     |
| 810 |   |  |     |
| 811 |   |  |     |
| 812 | Chuntao Yin, Yaqian Long, Lei Liu, Yasir Shaheen Khalil, and Songxing Ye. 2024a. Mapping ni-cu-platinum group element-hosting, small-sized, mafic-ultramafic rocks using worldview-3 images and a spatial-spectral transformer deep learning method. <i>Economic Geology</i> , 119(3):665–680.  |  |     |
| 813 |   |  |     |
| 814 |   |  |     |
| 815 |   |  |     |
| 816 |   |  |     |
| 817 |   |  |     |
| 818 | Shukang Yin, Chaoyou Fu, Sirui Zhao, Ke Li, Xing Sun, Tong Xu, and Enhong Chen. 2024b. A survey on multimodal large language models. <i>National Science Review</i> , page nwae403.   |  |     |
| 819 |   |  |     |
| 820 |   |  |     |
| 821 |   |  |     |
| 822 | Alex Young, Bei Chen, Chao Li, Chengen Huang, Ge Zhang, Guanwei Zhang, Heng Li, Jiangcheng Zhu, Jianqun Chen, Jing Chang, et al. 2024. Yi: Open foundation models by 01. ai. <i>arXiv preprint arXiv:2403.04652</i> .   |  |     |
| 823 |   |  |     |
| 824 |   |  |     |
| 825 |   |  |     |
| 826 |   |  |     |
| 827 | Yang Zhan, Zhitong Xiong, and Yuan Yuan. 2023. Rsvg: Exploring data and models for visual grounding on remote sensing data. <i>IEEE Transactions on Geoscience and Remote Sensing</i> , 61:1–13.  |  |     |
| 828 |   |  |     |
| 829 |   |  |     |
| 830 |   |  |     |
|     | Yang Zhan, Zhitong Xiong, and Yuan Yuan. 2024. Skyeyegpt: Unifying remote sensing vision-language tasks via instruction tuning with large language model. <i>arXiv preprint arXiv:2401.09712</i> .  |  | 831 |
|     |   |  | 832 |
|     |   |  | 833 |
|     |   |  | 834 |
|     | Daoan Zhang, Junming Yang, Hanjia Lyu, Zijian Jin, Yuan Yao, Mingkai Chen, and Jiebo Luo. 2024a. Cocot: Contrastive chain-of-thought prompting for large multimodal models with multiple image inputs. <i>arXiv preprint arXiv:2401.02582</i> .   |  | 835 |
|     |   |  | 836 |
|     |   |  | 837 |
|     |   |  | 838 |
|     |   |  | 839 |
|     | Duzhen Zhang, Yahan Yu, Jiahua Dong, Chenxing Li, Dan Su, Chenhui Chu, and Dong Yu. 2024b. Mm-llms: Recent advances in multimodal large language models. <i>arXiv preprint arXiv:2401.13601</i> .   |  | 840 |
|     |   |  | 841 |
|     |   |  | 842 |
|     |   |  | 843 |
|     | Wei Zhang, Miaoxin Cai, Tong Zhang, Yin Zhuang, and Xuerui Mao. 2024c. Earthgpt: A universal multimodal large language model for multi-sensor image comprehension in remote sensing domain. <i>IEEE Transactions on Geoscience and Remote Sensing</i> .   |  | 844 |
|     |   |  | 845 |
|     |   |  | 846 |
|     |   |  | 847 |
|     |   |  | 848 |
|     | Bingchen Zhao, Yongshuo Zong, Letian Zhang, and Timothy Hospedales. 2024. Benchmarking multi-image understanding in vision and language models: Perception, knowledge, reasoning, and multi-hop reasoning. <i>arXiv preprint arXiv:2406.12742</i> .   |  | 849 |
|     |   |  | 850 |
|     |   |  | 851 |
|     |   |  | 852 |
|     |   |  | 853 |
|     | Renguang Zuo. 2020. Geodata science-based mineral prospectivity mapping: A review. <i>Natural Resources Research</i> , 29(6):3415–3424.   |  | 854 |
|     |   |  | 855 |
|     |   |  | 856 |
|     | Renguang Zuo, Oliver P Kreuzer, Jian Wang, Yihui Xiong, Zhenjie Zhang, and Ziye Wang. 2021. Uncertainties in gis-based mineral prospectivity mapping: Key types, potential impacts and possible solutions. <i>Natural Resources Research</i> , 30:3059–3079.  |  | 857 |
|     |   |  | 858 |
|     |   |  | 859 |
|     |   |  | 860 |
|     |   |  | 861 |

## A Benchmark Construction

MineBench is based on the publicly available GSWA remote-sensing dataset, a reliable resource for geoscience applications. GSWA comprises 17 ASTER remote-sensing sub-datasets, 14 of which are synthesized using ASTER’s nine visible, near-infrared, and shortwave infrared bands (bands 1–9). The remaining three sub-datasets utilize ASTER’s thermal infrared bands (bands 10–14), extending the spectral range and enhancing suitability for geoscience interpretation. Each data underwent rigorous processing and evaluation to serve as the foundational base for MineBench.

**Data Collection** To identify the targeted deposits, we selected nine remote-sensing sub-datasets  $\mathcal{I}^a$  for analysis. The selected sub-datasets  $\mathcal{I}^a$  are categorized into two subsets based on their roles: geological images  $\mathcal{I}_a^{(g)}$  and hyperspectral images  $\mathcal{I}_a^{(h)}$ , as shown in Table 5. Details of these datasets are provided in the original technical document [Portal](#). The remote-sensing data were segmented into  $12 \times 12 \text{ km}^2$  areas using a grid method to facilitate detection. To ensure high-quality data, areas containing blurry, irrelevant images or those heavily affected by shadows obscuring geological features were excluded. After labeling, areas with mineral deposits near edges or other factors hindering accurate identification were excluded.

**Quality Control with Human Annotators.** A two-stage human review process was implemented to ensure data quality. A general reviewer conducted an initial quality check, followed by expert review and refinement. Areas requiring additional geochemical data or field observations for accurate identification were removed to improve prediction accuracy. This rigorous process ensures the accuracy and utility of MineBench.

## B Benchmark Preprocessing Workflow

A preprocessing workflow is proposed to construct the deposit signatures and mineral prospectivity map (MPM) used in MineBench evaluation and validation. This workflow enables precise control over feature extraction and integration, specifically optimized for copper mineralization detection. The detailed steps are as follows:

### B.1 Normalization of Remote-sensing Images

To ensure consistency and standardization, each remote-sensing image  $\mathcal{I}_a$  undergoes min-max nor-

malization:

$$\mathcal{I}_{a,\text{norm}} = \frac{\mathcal{I}_a - \min(\mathcal{I}_a)}{\max(\mathcal{I}_a) - \min(\mathcal{I}_a)} \quad (10)$$

where  $\min(\mathcal{I}_a)$  and  $\max(\mathcal{I}_a)$  are obtained from the original dataset (Table 6). This normalization scales remote-sensing images to the  $[0, 1]$  range, facilitating seamless integration in preprocessing steps. Additionally, the normalization function  $\text{norm}_{[a,b]}$  ensures a consistent scaling range throughout the workflow:

$$\text{norm}_{[\min, \max]}(\mathcal{I}_a) = \begin{cases} 0 & \text{if } x < \min \\ \frac{\mathcal{I}_a - \min}{\max - \min} & \text{if } \min \leq \mathcal{I}_a \leq \max \\ 1 & \text{if } x > \max \end{cases} \quad (11)$$

The function maps values to  $[0, 1]$ , capping outliers beyond specified bounds while preserving linear scaling within the target range. It improves the identification of high-potential areas by ensuring standardized and consistent data scaling.

### B.2 Preprocessing Step

**Deposit Signatures.** After normalization, raw hyperspectral images  $\mathcal{I}_a^{(h)}$  are transformed into deposit signatures  $\mathcal{I}_a^{(s)}$  using a weighted linear combination informed by domain-specific knowledge (Table 6). These relationships are critical for identifying regions with varying mineralization patterns. The first signature, the hydrothermal alteration zone  $\mathcal{I}_a^{(s,h)}$ , a primary indicator of copper mineralization, is computed as:

$$\mathcal{I}_a^{(s,h)} = \text{norm}_{[1,3]}(\mathcal{I}_a^{(h,ox)} + 2\mathcal{I}_a^{(h,oh)} + 4\mathcal{I}_a^{(h,op)}) \quad (12)$$

where  $\mathcal{I}_a^{(h,ox)}$  represents ferric oxide content,  $\mathcal{I}_a^{(h,oh)}$  denotes FeOH group content, and  $\mathcal{I}_a^{(h,op)}$  indicates the opaque index.  $\mathcal{I}_a^{(h,ox)}$ ,  $\mathcal{I}_a^{(h,oh)}$ , and  $\mathcal{I}_a^{(h,op)}$  are types of hyperspectral images associated with specific minerals. The weights 1, 2, and 4 reflect each indicator’s relative significance in identifying hydrothermal alteration. The normalization function scales the output to the range  $[1, 3]$ , enabling cross-regional comparisons and threshold-based targeting. The value range is derived from expert observations.

Similarly, the second signature, the propylitic alteration zone  $\mathcal{I}_a^{(s,p)}$ , which characterizes peripheral mineralization areas, is calculated as:

$$\mathcal{I}_a^{(s,p)} = \text{norm}_{[0.6,1]}(\mathcal{I}_a^{(h,al)} + \mathcal{I}_a^{(h,oh)} + \mathcal{I}_a^{(h,mg)} + 2\mathcal{I}_a^{(h,fe)}) \quad (13)$$

| Remote-sensing Data  | Associated Minerals                   | Geoscience Application   | Notion                   |
|----------------------|---------------------------------------|--|--------------------------|
| Ferric Oxide Content | Hematite, Goethite                    | Identifies oxidation zones within hydrothermal systems, where hematite and goethite accumulate due to surface weathering and high-oxidation conditions. Weakly associated with propylitic zones but commonly found in silicified zones within epithermal environments. | $\mathcal{I}_a^{(h,ox)}$ |
| FeOH Group Content   | Jarosite, Chlorite, Epidote           | Indicates FeOH-bearing minerals typical of acid-sulfate environments in hydrothermal systems. Strongly associated with propylitic alteration, with chlorite-epidote assemblages marking the transition between hydrothermal and propylitic zones.                      | $\mathcal{I}_a^{(h,oh)}$ |
| Opaque Index         | Magnetite, Pyrite, Manganese Oxides   | Highlights reduced zones containing opaque minerals like magnetite and pyrite. Primarily found in the core areas of hydrothermal systems and occasionally in overprinted propylitic zones.   | $\mathcal{I}_a^{(h,op)}$ |
| AlOH Group Content   | Muscovite, Kaolinite, Montmorillonite | Identifies AlOH-rich clays commonly associated with phyllic alteration in hydrothermal systems and transitional zones between phyllic and propylitic alteration.   | $\mathcal{I}_a^{(h,al)}$ |
| MgOH Group Content   | Chlorite, Epidote, Calcite            | Detects MgOH-bearing minerals, which form broad halos around hydrothermal zones as part of propylitic alteration. Typically shows an inverse correlation with silicification and is essential for mapping zonal alteration patterns.                                   | $\mathcal{I}_a^{(h,mg)}$ |
| Ferrous Iron Content | Chlorite                              | Primarily identifies iron-rich minerals within potassic zones of hydrothermal systems, including biotite and magnetite. Common in hydrothermal cores and useful for distinguishing primary iron minerals from secondary phases.  | $\mathcal{I}_a^{(h,fe)}$ |
| Quartz Index         | Quartz                                | Strongly correlated with silicification, particularly in quartz-dominant zones and silica-rich veins. Helps distinguish crystalline quartz from other forms of silica or silicates, such as feldspar, which is essential for mapping silicified alteration zones.      | $\mathcal{I}_a^{(h,qa)}$ |
| Silica Index         | SiO <sub>2</sub> , Quartz             | A key indicator of silicification, especially in advanced argillic zones of hydrothermal systems. Common in quartzite, silicified cap rocks, and vein systems.   | $\mathcal{I}_a^{(h,si)}$ |
| False Color Image    | Geological Environments               | Used to differentiate geological features from non-geological elements, such as vegetation, clouds, and shadows. Also serves as a greyscale or color background to visualize and interpret index-based alteration patterns.  | $\mathcal{I}_a^{(g)}$    |

Table 5: The details of nine remote-sensing data.

| MPM                                  | $\mathcal{I}_a^{(s)}$                         | $\mathcal{I}_a^{(h)}$ | Value Range of $\mathcal{I}_a^{(h)}$ | Weight of $\mathcal{I}_a^{(h)}$ | Weight of $\mathcal{I}_a^{(s)}$ |
|--------------------------------------|---|-----------------------|--------------------------------------|---------------------------------|---------------------------------|
| Copper Deposit<br>(Value Range: 0-5) | Geological Environment                        | False Color Image     | 0-1                                  | 1                               | 1                               |
|                                      | Hydrothermal Alteration<br>(Value Range: 1-3) | Ferric Oxide Content  | 1.1 – 2.1                            | 1                               | 5                               |
|                                      |   | FeOH Group Content    | 2.03 – 2.25                          | 2                               |                                 |
|                                      |   | Opaque Index          | 0.4 – 0.9                            | 4                               |                                 |
|                                      | Propylitic Alteration<br>(Value Range: 0.6-1) | AlOH Group Content    | 2.0 – 2.25                           | 1                               | 3                               |
|                                      |   | FeOH Group Content    | 2.03 – 2.25                          | 1                               |                                 |
|                                      |   | MgOH Group Content    | 1.05 – 1.2                           | 1                               |                                 |
|                                      |   | Ferrous Iron Content  | 0.1 – 2.0                            | 2                               |                                 |
|                                      | Silicification Zone<br>(Value Range: 1-3)     | Ferric Oxide Content  | 1.1 – 2.1                            | 1                               | 1                               |
|                                      |   | Quartz Index          | 1.0 – 1.35                           | 1                               |                                 |
| Silica Index                         |   | 0.5 – 0.52            | 2                                    |                                 |                                 |

Table 6: Weights and value ranges of deposit signatures and MPM in MineBench.

where  $\mathcal{I}_a^{(h,al)}$  represents AlOH group content,  $\mathcal{I}_a^{(h,mg)}$  indicates MgOH group content, and  $\mathcal{I}_a^{(h,fe)}$  denotes ferrous iron content.

The final signature, the silicification zone  $\mathcal{I}_a^{(s,s)}$ , which indicates secondary mineralization patterns, is quantified as:

$$\mathcal{I}_a^{(s,s)} = \text{norm}_{[1,2.5]}(\mathcal{I}_a^{(h,ox)} + \mathcal{I}_a^{(h,qa)} + 2\mathcal{I}_a^{(h,si)}) \quad (14)$$

where  $\mathcal{I}_a^{(h,qa)}$  represents quartz content and  $\mathcal{I}_a^{(h,si)}$  indicates silica abundance. This weighted combination captures distinct deposit signatures essential

for deposit detection.

**Mineral Prospectivity Map.** Following the weighted linear combination, the mineral potential map is constructed by combining deposit signatures  $\mathcal{I}_a^{(s,h)}$ ,  $\mathcal{I}_a^{(s,p)}$ , and  $\mathcal{I}_a^{(s,s)}$  to quantitatively evaluate the copper deposit potential based on the spatial distribution and intensity of key alteration zones:

$$\mathcal{I}_a^{(mpm)} = \text{normalize}_{[0,5]}(5\mathcal{I}_a^{(s,h)} + 3\mathcal{I}_a^{(s,p)} + \mathcal{I}_a^{(s,s)}) \quad (15)$$

The weights (5, 3, and 1) are derived from extensive statistical analysis of known copper deposits across

|      |   |   |
|------|---|---|
| 971  | diverse geological settings, reflecting the relative                                | 1021  |
| 972  | contribution of each zone to copper mineralization.                                 | 1022  |
| 973  | <i>Hydrothermal Alteration Zone.</i> The core zone                                  | 1023  |
| 974  | $\mathcal{I}_a^{(s,h)}$ is characterized by intense hydrothermal al-                | 1024  |
| 975  | teration and high-temperature mineral assemblages,                                  | 1025  |
| 976  | exhibiting the strongest spatial correlation with cop-                              | 1026  |
| 977  | per mineralization.   | 1027  |
| 978  | <i>Propylitic Alteration Zone.</i> Surrounding the hy-                              | 1028  |
| 979  | drothermal core, the intermediate zone $\mathcal{I}_a^{(s,p)}$ is                   | 1029  |
| 980  | characterized by moderate-temperature alteration                                    | 1030  |
| 981  | minerals, including chlorite, epidote, and calcite.                                 | 1031  |
| 982  | Although not directly mineralized, this zone pro-                                   | 1032  |
| 983  | vides critical context for delineating the extent of                                | 1033  |
| 984  | the hydrothermal system.  | 1034  |
| 985  | <i>Silicification Zone.</i> The outermost zone $\mathcal{I}_a^{(s,s)}$              | 1035  |
| 986  | is marked by silica enrichment and the presence                                     | 1036  |
| 987  | of low-temperature minerals. While less directly                                    | 1037  |
| 988  | associated with mineralization, this zone delineates                                | 1038  |
| 989  | system boundaries and fluid flow patterns.  | 1039  |
| 990  | This integrated approach highlights the hierar-                                     | 1040  |
| 991  | chical significance of different alteration signatures,                             | 1041  |
| 992  | improving the accuracy of copper mineral potential                                  | 1042  |
| 993  | assessments.  | 1043  |
| 994  | <b>B.3 Data Visualization</b>   | 1044  |
| 995  | Finally, we get three types of mineralogical data:                                  | 1045  |
| 996  | raw hyperspectral image $\mathcal{I}_a^{(h)}$ , deposit signatures                  | 1046  |
| 997  | $\mathcal{I}_a^{(s)}$ , and mineral prospectivity maps $\mathcal{I}_a^{(mpm)}$ . To | 1047  |
| 998  | enhance the interpretability of these data, we em-                                  | 1048  |
| 999  | ploy a visualization process comprising several key                                 | 1049  |
| 1000 | steps. First, we implement transparency for data                                    | 1050  |
| 1001 | points with zero normalized values, highlighting                                    | 1051  |
| 1002 | significant mineralization patterns. Second, we                                     |   |
| 1003 | overlay the mineralogical images on a grayscale                                     | <b>C Experimental Setting</b>                               |
| 1004 | geological image to provide geographic context.                                     | 1052  |
| 1005 | Finally, we apply a rainbow colormap to the nor-                                    | We accessed open-source models through API                  |
| 1006 | malized data, where warmer colors indicate higher                                   | services and closed-source models via their pre-            |
| 1007 | mineralization potential. This facilitates an intu-                                 | trained checkpoints, except for Qwen-72B which              |
| 1008 | itive interpretation of mineralization intensity and                                | was evaluated using its pretrained checkpoints. All         |
| 1009 | distribution. The resultant visualization enables a                                 | evaluations were conducted on two NVIDIA L40                |
| 1010 | clear understanding of potential copper deposits’                                   | (48GB) GPUs. To determine the parameter weights             |
| 1011 | intensity and spatial distribution through its color-                               | $w_i$ in Section 4.2.2, we employed five-fold cross-        |
| 1012 | coded representation.   | validation with Bayesian optimization and used the          |
| 1013 | <b>B.4 Data Validation</b>  | averaged weights across folds as the final param-           |
| 1014 | By carefully mapping color transitions from red to                                  | eters for MLLM evaluation. The resulting weight             |
| 1015 | yellow to orange and modulating spatial scales, we                                  | distributions are visualized in Figure 10. For the de-      |
| 1016 | created a nuanced visual representation of potential                                | defined classification tasks, we set a decision thresh-     |
| 1017 | mineral deposits. To ensure the reliability of our                                  | old of 3, $o^{(dm)}$ above this threshold are classified as |
| 1018 | synthetic data, we conducted a rigorous human-                                      | 1, otherwise as 0.  |
| 1019 | verified visual assessment. Expert manually ex-                                     | <b>D Score-Explanation Consistency</b>                      |
| 1020 | amined the spatial and chromatic characteristics,                                   | 1067  |
|      | comparing our synthetic mineralization patterns                                     | To evaluate the MLLMs’ reasoning ability, we ana-           |
|      | with ground truth deposit markers. This meticulous                                  | lyzed the alignment between scoring decisions $s_i$         |
|      | verification process confirmed the high correlation                                 |   |
|      | between our synthetic representations and actual                                    |   |
|      | mineral deposit locations.  |   |
|      | As shown in Figure 7, the synthetic mineral   |   |
|      | prospectivity maps reveal distinct patterns of min-                                 |   |
|      | eral potential. The authentic deposit locations                                     |   |
|      | (marked in red points) predominantly align with                                     |   |
|      | synthetic color-coded regions. Positive samples ex-                                 |   |
|      | hibit a gradual color transition from red to yellow to                              |   |
|      | orange, systematically capturing the alteration zone                                |   |
|      | characteristic of complete mineral deposits and re-                                 |   |
|      | fecting the continuous mineralization processes. In                                 |   |
|      | contrast, negative samples display markedly differ-                                 |   |
|      | ent characteristics, with either low color intensity                                |   |
|      | indicating minimal mineralization potential or an                                   |   |
|      | absence of complete color transitions suggesting                                    |   |
|      | incomplete deposit formation.   |   |
|      | For example, the positive sample (d) demon-   |   |
|      | strates a subtle but critical color gradient transi-                                |   |
|      | tioning, capturing the delicate mineralization pat-                                 |   |
|      | terns of mineral deposit. The scale of this sample,                                 |   |
|      | though small, precisely matches the actual deposit                                  |   |
|      | location markers. In contrast, the negative samples                                 |   |
|      | (c) and (d) exhibit significant differences. These                                  |   |
|      | regions feature large-scale, high-intensity red ar-                                 |   |
|      | reas that lack the nuanced color transitions and the                                |   |
|      | unnatural spatial distribution, immediately signal-                                 |   |
|      | ing these as potentially unreliable mineral deposit                                 |   |
|      | indicators.   |   |

and explanations  $e_i$  in Eq. 8 across three representative MLLMs: GPT-4o, Qwen-7B, and Yi-6B. Using t-SNE (Van der Maaten and Hinton, 2008) for visualization, the explanations are projected into BERT embeddings, with scores used as their labels for assessment. Based on identical scoring guidelines in the communication protocol, explanations  $e_i$  should be aligned with the scores  $s_i$ , resulting in a compact clustering pattern. Conversely, scattered distributions may indicate potential inconsistencies in the judging process (Du et al., 2024).

As shown in Figure 9, GPT-4o achieves superior clustering coherence, with distinct score-based clusters showing minimal boundary overlap. This clear structure indicates a strong alignment between scores and justifications, reflecting consistent reasoning patterns. Qwen-7B shows moderate clustering performance with distinguishable score groups but significant overlap in high-score regions (4-5), suggesting insufficient differentiation. Yi-6B exhibits the most dispersed distribution with minimal explanation-group separation, indicating weak alignment between scores and explanations. These clustering patterns correlate strongly with overall model performance, supporting our hypothesis that advanced models maintain more consistent score-explanation relationships.

## E Score Distribution of MLLMs and Human Assessment

Based on the score distribution visualization in Figure 8, we observe distinct patterns across human assessments and the two models (GPT-4o and Qwen-7b). GPT-4o’s score distribution closely aligns with human assessments, showing a more balanced and diverse distribution across different score levels. In contrast, Qwen-7b’s scores tend to concentrate around a single value, as evidenced by the sharp peaks in its distribution. This indicates a notable limitation of Qwen-7b in capturing nuanced distinctions in evaluation criteria, highlighting its reduced variability and less human-like reasoning capability compared to GPT-4o.

## F Impact of Decision-making Modules

**Impact of Assessment Tuples.** Multiple criteria in the assessment tuples  $C = \{c_1, c_2, \dots, c_M\}$  are used as input in the decision-making modules to guide the final decision  $o^{(dm)}$ , as shown in Eq.9. The various criteria contribute to robust reasoning compared to using a single criterion.

| Setting  | weights   | F1 (Pos.) | F1 (Avg.) | Roc-Auc | Mcc   |
|----------|-----------|-----------|-----------|---------|-------|
| Hard     | Local     | 24.86     | 34.4      | 58.81   | 12.94 |
|          | Mean      | 31.58     | 56.33     | 64.81   | 20.65 |
|          | Automatic | 36.51     | 60.47     | 68.63   | 27.07 |
| Standard | Local     | 31.82     | 49.6      | 69.03   | 24.71 |
|          | Mean      | 39.44     | 63.36     | 69.71   | 30.41 |
|          | Automatic | 61.20     | 77.19     | 83.35   | 56.30 |
| Easy     | Local     | 62.75     | 77.65     | 87.62   | 59.46 |
|          | Mean      | 67.13     | 81.40     | 80.84   | 62.82 |
|          | Automatic | 71.62     | 83.86     | 84.26   | 67.73 |

Table 7: Performance across different settings and weight allocation strategies.

To evaluate their impact  $o^{(dm)}$ , we employ three weighting strategies: (1) *Local* which focuses on three data-driven types: geological context  $c_1$ , hyperspectral context  $c_5$  and cross-reference validation  $c_6$  without intermediate results  $c_2-c_4$ ; (2) *Mean* which assigns equal weights to  $c_1-c_6$ ; and (3) *Automatic*, which dynamically balances criteria using Bayesian optimization.

As shown in Table 7, the *Local* setting obtained the worst accuracy due to the exclusion of  $c_2-c_4$ . In contrast, the *Mean* setting improved overall performance but failed to capture information hierarchies effectively. The *Automatic* setting achieved superior results through the dynamic integration of all available outputs, effectively ensuring high-confidence answers. These findings demonstrate that the decision-making modules enhance model robustness by considering multiple assessment criteria in a balanced manner.

**Impact of Decision-making Modules.** Figure 10 illustrates how the model adjusts its reliance on different criteria as task complexity increases. Each setting reveals unique patterns, highlighting the adaptive output of the decision-making module in response to varying levels of difficulty. In “Easy” tasks, the weights  $w_1$  to  $w_4$  for criteria  $c_1$  to  $c_4$  are relatively uniform, ranging from approximately 0.15 to 0.3. This balanced distribution reflects the model’s reliance on these single-category criteria for straightforward reasoning. The cross-image criterion  $c_5$  is assigned negligible weight, indicating its minimal contribution. This uniformity suggests that higher-order information integration is unnecessary for simple tasks, where single-category criteria alone suffice for accurate inference.

As tasks increase to “Standard” complexity, the weight distribution shifts toward more discrimina-

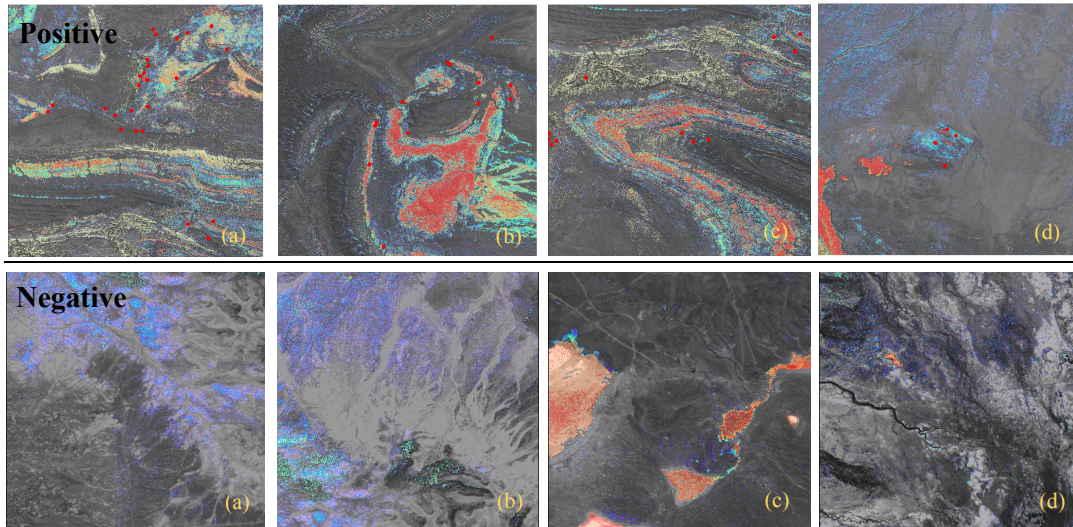


Figure 7: Data Validation. Comparing synthetic mineralization patterns with ground truth deposit locations.

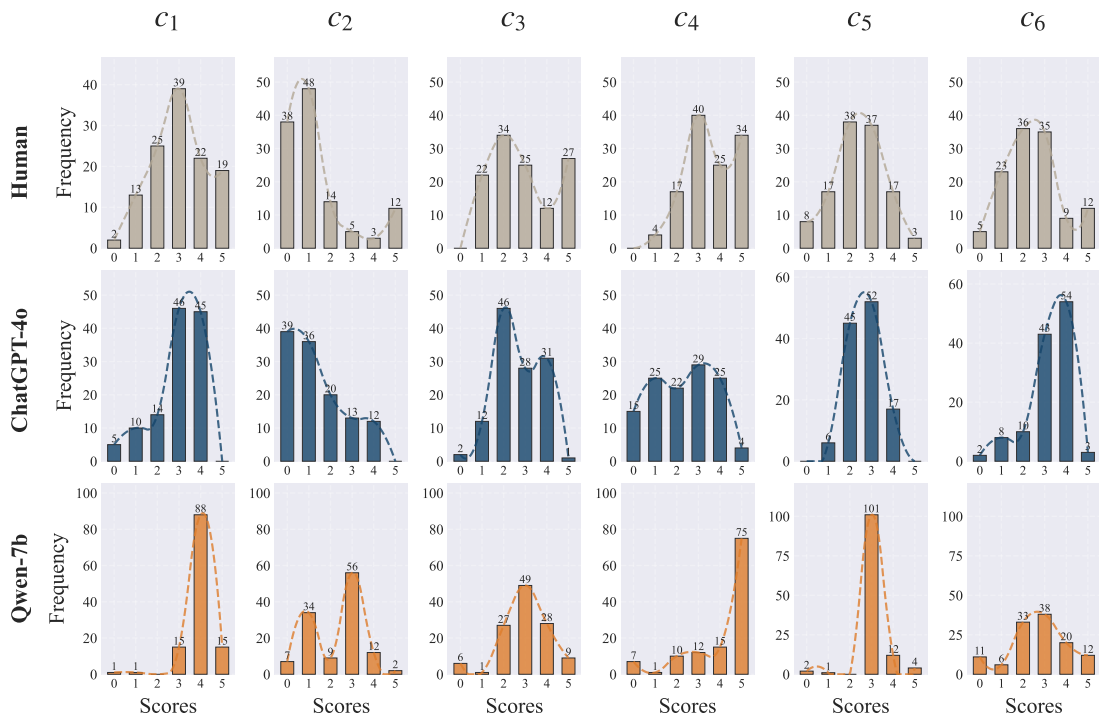


Figure 8: Score Distribution of MLLMs and Human Assessment

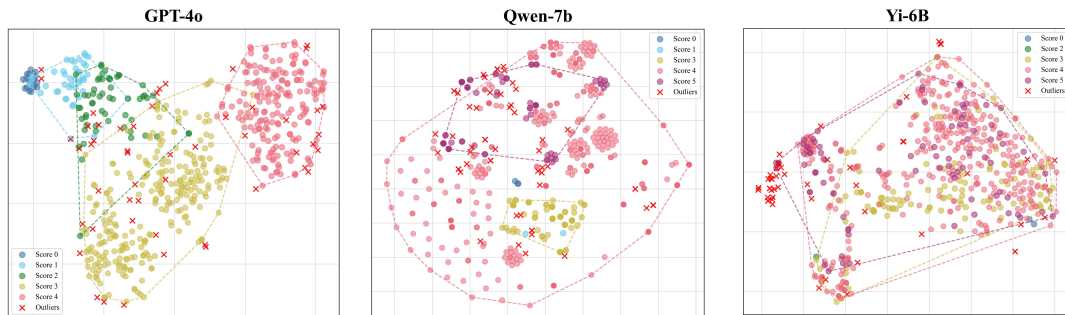


Figure 9: Visualization of score-explanation alignment using T-SNE projection. Data points are color-coded by scores ranging from 0 to 5, with red crosses marking statistical outliers. Ideally, the explanation should be consistent with the assigned scores, leading to the clustering patterns.

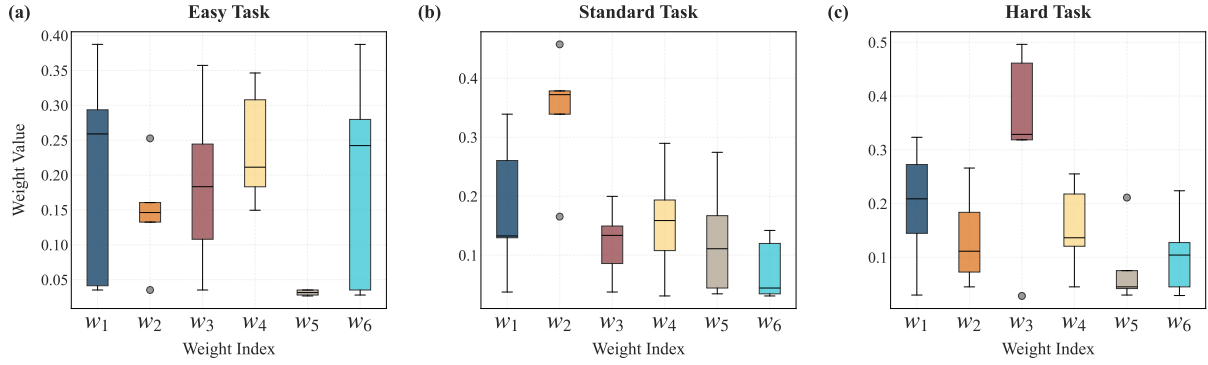
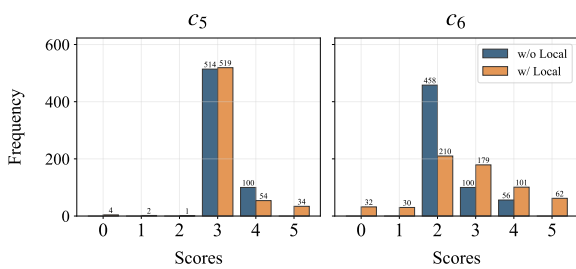


Figure 10: The Parameters of Decision-making Modules.  $w_1$  to  $w_6$  are assigned to various criterias ( $c_1$  to  $c_6$ ) across three task settings. Each box represents the range of weight values.

1156 tive features. For instance,  $w_2$  increases significantly to approximately 0.5, underscoring its role as a key criterion. While cross-image criteria gain slightly more weight, they remain secondary as the model integrates aggregated insights alongside foundational criteria. Notably, single-category criteria continue to dominate the reasoning process in this setting.

1157  
1158  
1159  
1160  
1161  
1162  
1163  
1164 In “Hard” tasks, the model heavily relies on a few single-category criteria (e.g.,  $w_1$  and  $w_3$ ), while cross-image criteria ( $w_5$  and  $w_6$ ) maintain negligible contributions. This reflects their reduced utility as task complexity increases, further emphasizing the importance of individual, highly discriminative criteria for complex reasoning.

## 1164 G Effectiveness of Cross-image Tools



1165  
1166  
1167  
1168  
1169  
1170  
1171 Figure 11: Effectiveness of cross-image tools. The impact of including/excluding additional references as input on the score distribution for global criteria  $c_5$  and  $c_6$ , evaluated using Qwen-7B.

1172 As shown in Table 1, cross-image tools leverage inferences from single-category tools to analyze complex relationships between multiple images. This integration harnesses complementary strengths, resulting in a balanced score distribution that reflects improved model robustness across diverse inference tasks. Figure 11 demonstrates

1179 that removing single-category inferences leads to a more concentrated score distribution, indicating that the model struggles to capture nuanced image features without auxiliary inputs. In contrast, integrating these inferences significantly improves the score distribution by increasing the proportion of high-scoring regions and reducing low-scoring instances. This improvement highlights enhanced reasoning accuracy. These findings emphasize the critical role of hierarchy flow in judging modules in strengthening inference robustness. By combining both global and detailed perspectives, the judging modules establish a more reliable reasoning for addressing cross-image reasoning challenges.

## 1193 H The Exploration Pipeline and Case Study

1194  
1195  
1196  
1197  
1198  
1199  
1200  
1201  
1202  
1203 The detailed pipelines for the “Easy,” “Standard,” and “Hard” settings are shown in Figure 12 13 and 14, respectively. The “Standard” and “Hard” pipelines differ only in the design of the hyperspectral tools. Consequently, the “Hard” pipeline focuses exclusively on the hyperspectral tools segment. For each setting, a case study is provided to illustrate the reasoning process in action, as shown in Figure 15 16 and 17.

## 1204 I More Related Work

1205  
1206  
1207  
1208  
1209  
1210  
1211  
1212  
1213 **Machine Learning for Mineral Exploration.** Mineral exploration represents a complex classification problem in geoscience, integrating diverse data sources to predict the location, quantity, and quality of mineral deposits (Carranza, 2008). Over the years, machine learning (ML) has played a transformative role in this field. Traditional approaches, such as principal component analysis (Ousmanou et al., 2024), k-means (Ren et al.,

### ### Instructions for Cross-image Tools

You are a mineral exploration expert tasked with evaluating the potential for copper deposits in a given area using remote sensing images. Follow the three-step process below, ensuring the evaluation strictly adheres to the outlined criteria.

#### ### Step 1: Initial Analysis - False Color Image Analysis

Goal: Identify key surface features such as exposed bedrock, vegetation, and water bodies to establish a foundation for further mineral index analysis.

##### Procedure:

###### 1.1 Identify Exposed Bedrock:

- Focus on brown and gray areas in the image, which usually represent exposed bedrock or alteration zones, indicating potential copper mineralization areas.

###### 1.2 Exclude Non-Target Areas:

- Exclude green and blue areas, representing vegetation and water bodies, as they are less likely to be associated with copper mineralization.

###### 1.3 Identify Linear Structures:

- Look for faults, fractures, and other linear features, as these may serve as conduits for hydrothermal fluids, which are typically linked to copper mineralization.

#### ### Step 2: Mineralization Potential Map Analysis

Goal: Further refine the areas identified in Step 1 using the Mineralization Potential Map. For an area to be considered a strong copper deposit candidate, it must show continuous red, yellow/orange, and green/blue regions. Any area missing one or more of these colors or without a smooth gradient should be excluded.

##### Procedure:

###### 2.1 Hydrothermal Alteration (Red Areas):

- Red areas indicate intense hydrothermal activity, rich in minerals like magnetite and hematite, typically linked to copper deposit cores. Only red areas that smoothly transition into yellow/orange and green/blue zones should be considered.

###### 2.2 Propylitic Alteration (Yellow/Orange Areas):

- Yellow/orange areas signify lower-temperature propylitic alteration, found in the outer zones of a mineralization system. These areas must be adjacent to red zones to be considered part of a copper deposit system.

###### 2.3 Silicification Zones (Green/Blue Areas):

- Green/blue areas are rich in silica, potentially indicating secondary mineralization such as quartz veins. Only these areas that show a smooth transition from the yellow/orange zones should be considered for further evaluation.

#### ### Step 3: Correlation and Continuity Analysis

Goal: Evaluate the spatial continuity between the mineralization core, outer alteration zones, and silicified areas to determine copper deposit potential.

##### Procedure:

###### 3.1 Assess Spatial Continuity:

- Ensure that the red core zones smoothly transition into yellow/orange alteration zones and then into green/blue silicified zones. This transition must be continuous and cover a sufficiently large area to suggest the presence of a cohesive mineralization system.

###### 3.2 Evaluate Gradient and Area Coverage:

- Verify that the transition from red to yellow/orange to green/blue is smooth and covers a significant area. Disconnected color patches should be excluded unless they are part of a larger continuous system.

---

#### ### Scoring Guidelines (0-20 Points):

Score the potential mineralization zones based on the following criteria:

##### Confidence 1: Geological context(0-4 points):

- Award points based on the presence and extent of favorable geological features, such as exposed bedrock or linear structures.

##### Confidence 2: Deposit signatures Identification (0-8 points):

- Hydrothermal Alteration (0-4 points): Score based on the clarity and size of red areas and ensure that they transition smoothly into yellow/orange and green/blue areas.
- Propylitic Alteration (0-2 points): Award points if yellow/orange areas are adjacent to red areas and form a continuous system.
- Silicification Zone (0-2 points): Award points if green/blue areas follow the yellow/orange zones with a smooth transition.

##### Confidence 3: Relation between deposit signatures (0-4 points):

- If red, yellow/orange, and green/blue areas are all present, evaluate their connection. Award points based on the smoothness and continuity of transitions across the zones. If they are not connected, assign 0 points.

##### Confidence 4: Cross-referencing Validation (0-4 points):

- Compare the Mineralization Potential Map with the favorable geological features from the False Color Image. Award high points if the areas identified in both analyses overlap significantly. Adjust points downward if there is overlap with non-target areas such as water bodies or dense vegetation.

#### ### Final Assessment:

- Total Score: Sum the confidence scores. Areas with a total score greater than 16 suggest significant copper mineralization potential and should be prioritized for further exploration.

#### ### Important Reminder:

Ensure all analyses focus on areas displaying continuous red, yellow/orange, and green/blue gradients. The scoring system must be applied consistently to maintain the accuracy of the results. Do not deviate from this process unless justified by specific data.

Figure 12: The pipeline of “Easy” setting

### ### Instruction for Geological Tool

As a geological expert, your task is to evaluate the copper deposit potential based on a False Color Image (FCC). Focus on identifying favorable geological areas like exposed bedrock and linear structures. Analyze the image and assign a score from 0 to 5 based on the potential for copper mineralization.

#### Procedure:

1. Identify Exposed Bedrock:
  - Focus on brown and gray areas in the image, which usually represent exposed bedrock or alteration zones, indicating potential copper mineralization areas.
2. Exclude Non-Target Areas:
  - Exclude green and blue areas, representing vegetation and water bodies, as they are less likely to be associated with copper mineralization.
3. Identify Linear Structures:
  - Look for faults, fractures, and other linear features, as these may serve as conduits for hydrothermal fluids, which are typically linked to copper mineralization.

#### ### Scoring Guidelines for Geological Context (0-5 points):

- 0 Points: No favorable geological features (e.g., bedrock, linear structures); Image dominated by vegetation or water bodies.
- 1-2 Points: Limited favorable features, such as small or isolated bedrock areas; Few or poorly connected linear structures. Low potential for copper mineralization.
- 3 Points: Moderate presence of exposed bedrock and identifiable linear structures; Some overlap between favorable areas, but the overall zone size is limited. - Medium potential for copper deposits.
- 4 Points: Well-distributed bedrock areas and several linear structures; High potential for copper deposits, with strong indicators but minor uncertainty.
- 5 Points: Large, continuous bedrock areas with multiple well-defined linear structures; Strong spatial continuity, indicating very high potential for copper mineralization. Set this score if the image is highly favorable overall.

### ### Instructions for Hyperspectral Tools

As a mineral exploration expert, your goal is to evaluate the copper deposit potential in a given area. The analysis focuses on the colored areas in the images, where red represents high values and blue represents low values, following a rainbow color scale. Your objective is to identify and describe potential mineralization areas based on both the intensity (color value) and the size of the colored regions. Assign a score between 0 and 5 to each mineral index.

#### Procedure:

You will analyze three key mineral indices based on the color distribution:

1. Hydrothermal Alteration: Indicates core zones of copper deposits, linked to strong hydrothermal activity.
2. Propylitic Alteration: Typically represents outer edges of the mineral system with low-temperature alteration.
3. Silicification Zone: Indicates areas rich in quartz veins, commonly associated with copper mineralization.

#### ### Scoring Guidelines for Deposit Signatures (0-5 Points)

- 0 Points: No significant colored areas. Set "favorable\_area" to "no favorable area". No potential.
- 1 Points: Scattered high-value areas or moderate low-value areas. Low potential for mineralization.
- 2 Points: Small high-value areas or well-distributed low-value areas. Low potential for mineralization.
- 3 Points: Moderate high-value areas with well-distributed low values. Some potential for mineralization.
- 4 Points: Well-distributed high-value areas with large spatial coverage. High potential for mineralization.
- 5 Points: Large, continuous high-value areas. Strong mineralization potential due to size and intensity. High potential for mineralization.

#### ### Important Reminder:

- High-value colored areas (red, yellow, green) in the image should be prioritized, with larger areas indicating higher potential.
- Color Bar for Reference
  - Blue Areas: Indicate low values; Green Areas: Represent moderate-low values; Yellow Areas: Indicate intermediate values
  - Orange Areas: Represent moderately high values; Red Areas: Represent high values.

### ### Instructions for Cross-image Tools

As a remote sensing image analysis expert, your task is to identify favorable areas for copper mineralization by analyzing the provided images. Focus on two main tasks, and base your scoring solely on image overlay to locate areas with the highest potential for copper deposits. Assign a score between 0 and 5 to each task.

#### ### Procedure:

1. Assess Mineral Indices: Analyze the Hydrothermal Alteration, Propylitic Alteration, and Silicification Zone to evaluate the continuity of mineralization features.
  - Focus on high-value areas (red and other strong colors) in the images.
  - Identify where these areas overlap or are close to each other across the three indices.
  - Look for continuity: smooth transitions from hydrothermal zones to propylitic and silicification zones.

#### ### Scoring Guidelines for Signatures' Relation (0-5 Points)

- 0 Points: No observable continuity or overlap of colored areas across all indices.
- 1 Points: Weak continuity and minimal overlap of colored areas across all indices.
- 2 Points: Weak continuity with some overlap of colored areas across all indices.
- 3 Points: Moderate continuity with some overlap of colored areas across all indices.
- 4 Points: Moderate continuity with some overlap of high-value areas across all indices.
- 5 Points: Strong continuity with some overlap of high-value areas across all indices.

#### ### Procedure:

2. Identify the Final Favorable Location: Find where geological insight from FCC overlap with the high-potential mineral areas identified in the first task.

#### - Instructions:

- Locate the high-potential mineral areas identified in the first task "Assess Mineral Indices".
- Locate favorable geological insight in the false color composition image.
- Cross-reference these geological features with the high-potential zones derived from the "Assess Mineral Indices".
- Highlight regions where geological features and high-potential mineralization areas coincide, as these are the most promising locations for copper deposits.

#### ### Scoring Guidelines for Cross-referencing Validation (0-5 Points)

- 0 Points: No significant mineralization features identified from task 1 or geological insight from the FCC.
- 1 Points: No significant overlap between mineralization features from task 1 and geological features from the FCC.
- 2 Points: Minimal overlap between mineralization features from task 1 and geological features from the FCC.
- 3 Points: Moderate overlap between mineralization features from task 1 and geological features from the FCC.
- 4 Points: Significant overlap in moderate-potential areas between mineralization features from task 1 and favorable geological features from the FCC.
- 5 Points: Significant overlap in well-distributed potential areas between mineralization features from task 1 and favorable geological features from the FCC.

Figure 13: The pipeline of "Standard" setting

### ### Instructions for Hyperspectral Tools

As a mineral exploration expert, your goal is to assess the copper deposit potential in a designated region by analyzing mineral indices images. This process is carried out in two stages: 1. Analyze individual mineral index images separately. 2. Perform a combined analysis by integrating the results of these individual indices. Each step focuses on the colored areas in the images. After combining the indices, you will assign a score between 0 and 5 for each zone.

#### Procedure:

##### 1. Analysis of Individual Hyperspectral Images:

In this stage, you will analyze each Mineral Index based on the color distribution in the image:

- Ferric Oxide Index (Hematite, Goethite): Highlights iron oxide-rich zones, commonly associated with copper deposit cores.
- FeOH Group Index (Chlorite, Epidote, Jarosite): Identifies FeOH-rich zones, often found in outer hydrothermal alteration zones.
- Opaque Index: Detects opaque minerals (e.g., magnetite), often present in copper mineralization cores.
- AlOH Group Index (Muscovite, Illite, Kaolinite): Detects sericitic alteration, typically found in outer copper deposit zones.
- MgOH Group Index (Chlorite, Calcite, Dolomite): Indicates magnesium-rich alteration from low-temperature hydrothermal fluids.
- Ferrous Iron in MgOH Index (Chlorite, Actinolite): Suggests peripheral mineralization in copper systems.
- Quartz Index: Highlights quartz veins, commonly linked to hydrothermal systems.
- Silica Index: Identifies silicified zones, which are often associated with mineralized areas.

For each index, you will evaluate copper potential by assessing the intensity and the spatial distribution of high-value areas.

##### 2. Combined Deposit Signatures Analysis:

After individually analyzing each Mineral Index, combine the results to get a comprehensive view.

###### 2.1 Hydrothermal Alteration Zones:

- Indicators: High-value areas in the Ferric Oxide, FeOH Group, and Opaque indices suggest high-temperature hydrothermal activity and copper mineralization cores.
- Significance: These are the primary mineralization targets and should be the main focus of exploration.

###### 2.2 Propylitic Alteration Zones:

- Indicators: High-value areas in the AlOH, FeOH, MgOH, and Ferrous Iron indices suggest outer alteration zones influenced by low-temperature hydrothermal fluids.
- Significance: These areas often indicate peripheral or secondary mineralization potential, providing key insights into the broader mineral system.

###### 2.3 Silicification Zones:

- Indicators: High-value areas in the Ferric Oxide, Quartz, and Silica indices suggest the presence of quartz veins or silicified zones, often linked to secondary mineralization.
- Significance: These areas provide additional clues to copper mineralization near the outer limits of the system.

After identifying these zones, provide a score based on their spatial distribution, continuity, and overall potential for copper deposits.

### ### Scoring Guidelines for Deposit Signatures (0-5 Points)

- 0 Points: No significant potential areas across the combined mineral indices. Set "favorable\_area" to "no favorable area". No potential.
- 1 Points: A few scattered potential areas across the combined indices. Very low mineralization potential.
- 2 Points: A few small, isolated potential areas across the combined indices. Low mineralization potential.
- 3 Points: Moderate potential areas across the combined indices. Some copper potential. Some potential.
- 4 Points: Well-distributed potential areas across the combined indices. High potential.
- 5 Points: Large, continuous potential areas across the combined indices. Very High potential.

### ### Important Reminder:

- High-value colored areas (red, yellow, green) in the image should be prioritized, with larger areas indicating higher potential.
- Color Bar for Reference
  - Blue Areas: Indicate low values;
  - Green Areas: Represent moderate-low values;
  - Yellow Areas: Indicate intermediate values
  - Orange Areas: Represent moderately high values;
  - Red Areas: Represent high values.

Figure 14: The pipeline of "Hard" setting



<False color image><Mineral Prospectivity Map>

**MineAgent:** You are a mineral exploration expert tasked with evaluating the potential for copper deposits in a given area using remote sensing images. Score the potential mineralization zones based on the following guideline.

1. Provide a certainty score from 0 to 20, reflecting the overall confidence in your decision.
2. Assign a label of 1 (presence of copper deposits) only if there is strong evidence, such as high confidence or clear mineralization patterns. If the evidence is insufficient, assign a label of 0 (absence of copper deposits).
3. Evaluate each factor carefully, step by step, before making your final conclusion.

**Output:** {"prediction": 1, "score": 18.0, "explanation": "The false color image shows significant areas of exposed bedrock, particularly along the central and eastern parts of the image, which are potential indicators of copper mineralization. Linear structures, such as faults and fractures, are also visible, which can serve as conduits for hydrothermal fluids. The mineral prospectivity map shows a strong presence of red, yellow/orange, and green/blue areas, indicating hydrothermal alteration, propylitic alteration, and silicification zones, respectively. These areas are continuous and show smooth transitions between them, especially in the central and eastern parts of the image. Based on the explanation, the region shows significant potential for copper deposits, with a total score of 18. The presence of favorable geological features, continuous mineralization zones, and smooth transitions between these zones support the high potential for copper mineralization."}

Figure 15: The example of "Easy" setting



<False color image>

**Geological Tool:** As a geological expert, your task is to evaluate the copper deposit potential based on a False Color Image (FCC). Focus on identifying favorable geological areas like exposed bedrock and linear structures. Analyze the image and assign a score from 0 to 5 based on the potential for copper mineralization.

**c1:** {"score": 4, "favorable\_area": "Central and eastern regions with exposed bedrock and linear structures", "explanation": "The image shows significant areas of brown and gray, indicating exposed bedrock, particularly in the central and eastern parts. There are also several linear features that suggest the presence of faults or fractures, which are favorable for copper mineralization. The distribution and size of these features indicate a high potential for copper deposits, with strong geological indicators present."}



<Hydrothermal\_Alteration>



<Propylitic\_Alteration>



<silicification zone>

**Hyperspectral Tools:** As a mineral exploration expert, your objective is to identify and describe potential mineralization areas based on both the intensity (color value) and the size of the colored regions. Assign a score between 0 and 5 to each mineral index. You will analyze three key mineral indices based on the color distribution:

1. hydrothermal alteration: High-value areas in the Ferric Oxide, FeOH Group, and Opaque indices suggest high-temperature hydrothermal activity and copper mineralization cores.
2. propylitic alteration: High-value areas in the AlOH, FeOH, MgOH, and Ferrous Iron indices suggest outer alteration zones influenced by low-temperature hydrothermal fluids.
3. silicification zone: High-value areas in the Ferric Oxide, Quartz, and Silica indices suggest the presence of quartz veins or silicified zones, often linked to secondary mineralization.

**c2:** {"score": 4, "favorable\_area": "The hydrothermal alteration zone shows well-distributed high-value areas, particularly along the central and northern sections, with significant red and orange regions., "explanation": "The presence of continuous red and orange areas indicates a high potential for copper mineralization due to strong hydrothermal activity."}

**c3 :** {"score": 3, "favorable\_area": "The propylitic alteration zone has scattered moderate to high-value areas, with some orange and yellow regions mainly in the central part., "explanation": "The distribution of orange and yellow areas suggests moderate potential for mineralization, indicating peripheral zones of the mineral system."}

**c4:** {"score": 2, "favorable\_area": "The silicification zone has small, scattered high-value areas with limited orange and yellow spots., "explanation": "The limited size and distribution of high-value areas suggest low to moderate potential for copper mineralization. The areas are not extensive enough to indicate strong mineralization potential."}



<False color>



<Hydrothermal\_Alteration>



<Propylitic\_Alteration>



<silicification zone>

**Cross-image Tools:** As a remote sensing image explanation expert, your task is to identify favorable areas for copper mineralization by analyzing the provided images. Focus on two main tasks, and base your scoring solely on image overlay to locate areas with the highest potential for copper deposits. Assign a score between 0 and 5 to each task.

1. Based on the above analyses from {c1,c2,c3}, ensure that core zones transition smoothly into propylitic zones and then into silicified zones.
2. Based on the above analyses {c1,c2,c3} and {c1}, find where geological features overlap with the high-potential mineral features.

**c5:** {"score": 4, "favorable\_area": "Central region with overlapping hydrothermal and propylitic alteration, "explanation": "The central region shows strong continuity of high-value areas in both hydrothermal and propylitic alteration zones, with significant red and orange areas indicating potential copper mineralization. This suggests a high potential due to the presence of continuous alteration features."}

**c6:** {"score": 4, "favorable\_area": "Central and eastern regions with exposed bedrock and alteration overlap", "explanation": "The central and eastern regions show a significant overlap of geological features from the FCC image, such as exposed bedrock and linear structures, with high-value alteration zones. This overlap suggests a strong potential for copper deposits, as geological and mineral indices align well."}

Figure 16: The example of “Standard” setting

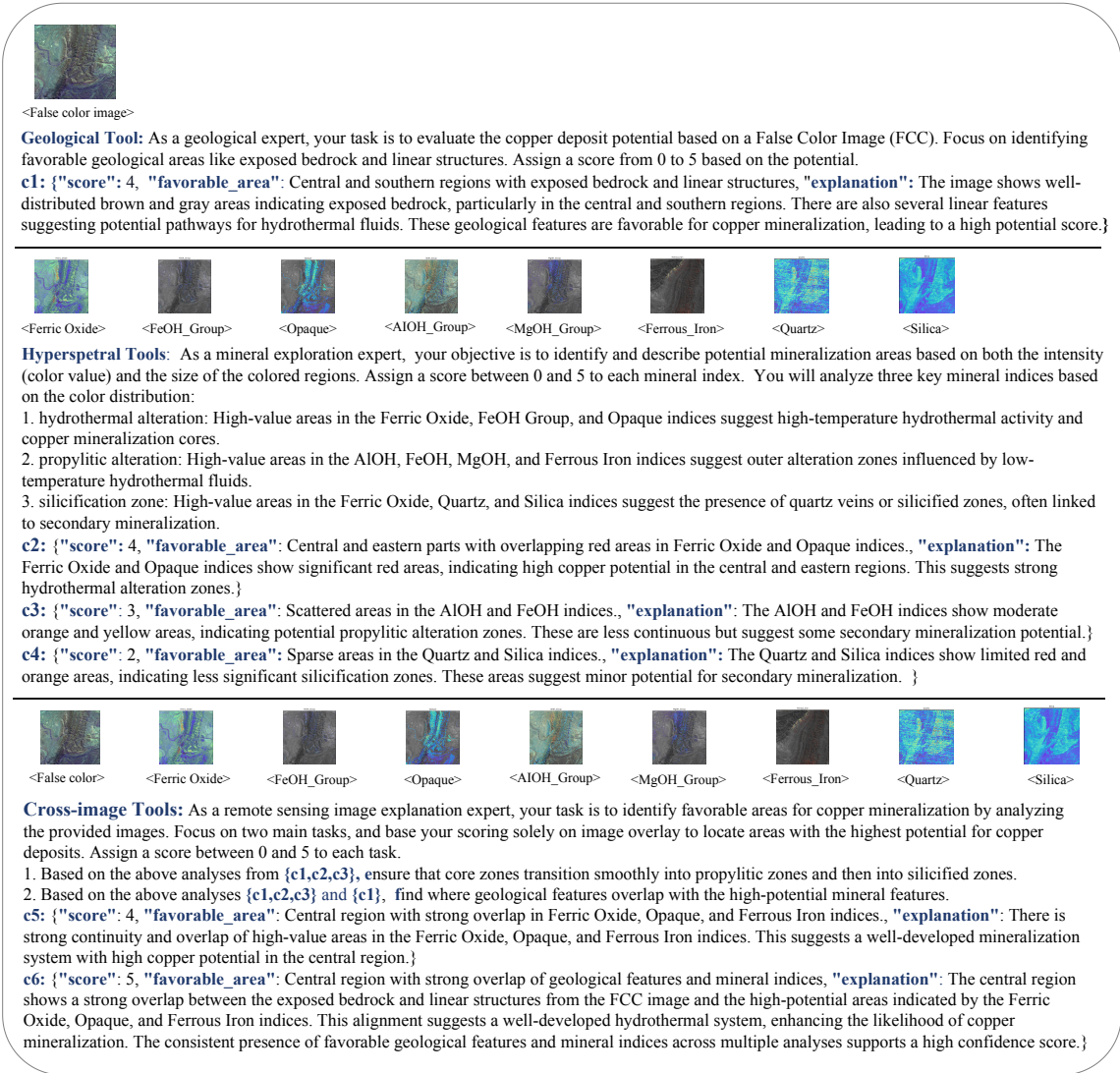


Figure 17: The example of “Hard” setting

1214 2020), and regression trees (Pham et al., 2018),  
1215 have shown success in identifying prospective min-  
1216 eral deposits. With the increasing complexity of  
1217 remote-sensing data, deep learning (DL) models  
1218 have demonstrated efficient and accurate feature ex-  
1219 traction capabilities (Liu et al., 2023a; Yang et al.,  
1220 2024). However, existing ML and DL methods face  
1221 key limitations, including dependence on labeled  
1222 datasets and poor generalizability across diverse  
1223 geological environments. To address these chal-  
1224 lenges, we propose leveraging advanced MLLMs  
1225 to explore mineral deposits, integrating human ex-  
1226 pertise for enhanced insights.